GNG-2018003

Assessment of Microbial Contamination Probability for Sample Return from Martian Moons

Kazuhisa Fujita
Institute of Space & Astronautical Science, Japan Aerospace Exploration Agency

Kosuke Kurosawa
Planetary Exploration Research Center, Chiba Institute of Technology

Hidenori Genda, Ryuki Hyodo
Earth-Life Science Institute, Tokyo Institute of Technology

Takashi Mikouchi
The University Museum, The University of Tokyo

Shingo Matsuyama
Institute of Aerospace Technology, Japan Aerospace Exploration Agency

and

Phobos/Deimos Microbial Contamination Assessment Team
Japan Aerospace Exploration Agency

Change Records

Issue	Date	Change records	Author
First issue	4/09/2018		Fujita et al.

Abstract

Potential microbial contamination of Martian moons (Phobos and Deimos), which can be brought about by transportation of Mars ejecta produced by meteoroid impacts on the Martian surface, has been comprehensively assessed in a statistical approach, based on the most probable history of recent major gigantic meteoroid collisions on the Martian surface. The fundamental data, such as the microbial survival rates against hypervelocity impact and solar and galactic cosmic radiation, are taken from the preceding study of SterLim (ESA contract no. 4000112742/14/NL/HB), while some additional physical processes and numerical approaches are newly introduced to accomplish more detailed and realistic assessment of microbial contamination. Potential microbial density on the Martian surface as the source of microorganisms is revised by analogy from the terrestrial areas having the similar arid and cold environments. Mars ejecta transportation from the Martian surface and impact onto the Martian moons are numerically simulated by the Smoothed Particle Hydrodynamics (SPH) method and associated trajectory analysis in a Monte Carlo manner, taking sterilization into consideration, to obtain statistical assessment of the microbial density survived on the current surface of the Martian moons. Hypervelocity impact and radiation are major causes to annihilate potential microorganisms transported to the surface of the Martian moons. It is pointed out that the microbial survival rate against hypervelocity impact should be extended to a higher velocity range, since the major portion of Martian ejecta are found to impact on Phobos at the velocities higher than those tested in the SterLim study. Since radiation sterilization progresses with time, the Martian crater events that occurred before 2 Myr and in earlier ages have little effect on the microbial density on the current surface of the Martian moons. The potential microbial density on the surface of Phobos and Deimos has been updated, and the potential spatial distributions, which is due to revolution of the Martian moons around Mars, are obtained as well. Finally, the microbial contamination probability of collected samples is estimated for several types of sampling methods. It has been found that the microbial contamination probability of collected samples can be maintained below 10^{-6} by a variety of sampling manners. The microbial transfer model is applied to natural transfer of microbes by Martian meteorites as well. It is found that microbial contamination probability due to natural transfer by Martian meteorite is several orders of magnitude higher than that of sample return from the Martian moons, suggesting an apparent evidence of a natural influx from Mars including viable microbes. From the above results, sample return from the Martian moons can be classified as Unrestricted Earth return.

Contents

1. Introduction

1.1. Purpose and Scope

The purpose of this study is to clarify the potential physical processes which can bring about microbial contamination on the surface of Martian moons, Phobos and Deimos, to obtain a quantitative estimate of the density of microorganisms still surviving in the regolith of the Martian moons through several sterilization processes, and to assess microbial contamination probability of samples collected on the surface of the Martian moons for future sample return missions from the Martian moons.

According to COSPAR Planetary Protection Policy (PPP), the probability that a single unsterilized particle from Mars ≥ 10 nm in diameter is in a sample returned from Phobos shall be ≤ 1×10^{-6} (REQ-10). Microbial contamination probability is assessed in the criteria whether REQ-10 is fulfilled or not.

This work is an extension of the preceding study, SterLim (ESA contract no. 4000112742/14/NL/HB) (Patel et al. 2018; Summers 2017). More detailed information about the physical processes and numerical procedures introduced in this study may be found in another article (Genda et al. in prep.; Kurosawa et al. in prep.; Hyodo et al. in prep.).

1.2. Definitions and Acronyms

CFD	Computer Fluid Dynamics
CFU	Colony Forming Unit
SFD	Size-Frequency Distribution
SPH	Smoothed Particle Hydrodynamics
TC	Time Constant, the time needed to sterilize microorganisms by 1/e

2. Overview of Microbial Contamination of Martian Moons

2.1. Potential Scenario of Microbial Contamination

A potential scenario of microbial contamination of the Martian moons is illustrated in Fig.2-1. Following the SterLim study, we consider that microbes, which potentially exist on the Martian surface (denoted as 1 in Fig.2-1.), are transported to the Martian moons by Mars ejecta produced by meteoroid impacts on the Martian surface (2). Some portions of microbes are annihilated through hypervelocity impacts during Mars ejecta formation (3) and aerodynamic hearing acting on Mars ejecta during hypersonic flight in the Martian atmosphere (4). Mars ejecta that are potentially contaminated with Martian microbes are transported to orbits of the Martian moons, a small portion of which may impact against the Martian moons, destroyed into fragments with considerable shock-heating. Because of such shock-heating, a considerable portion of microbes contained in the Mars ejecta are annihilated (5). A certain portion of the Mars ejecta fragments are considered to remain in the craters on the surface of the Martian moons, and to be diluted with indigenous fragments, forming a collapsed lens (see Section 9.1 in detail) of considerable thickness. On the other hand, the rest of the Mars ejecta fragments and some portion of the indigenous fragments, both of which are small in diameter, are ejected into orbits around Mars, and finally re-impact on the global surface of the Martian moons, forming a contaminated layer of submillimeter thickness (6). These processes are illustrated in more detail in Figs. 2-2a and 2-2b.

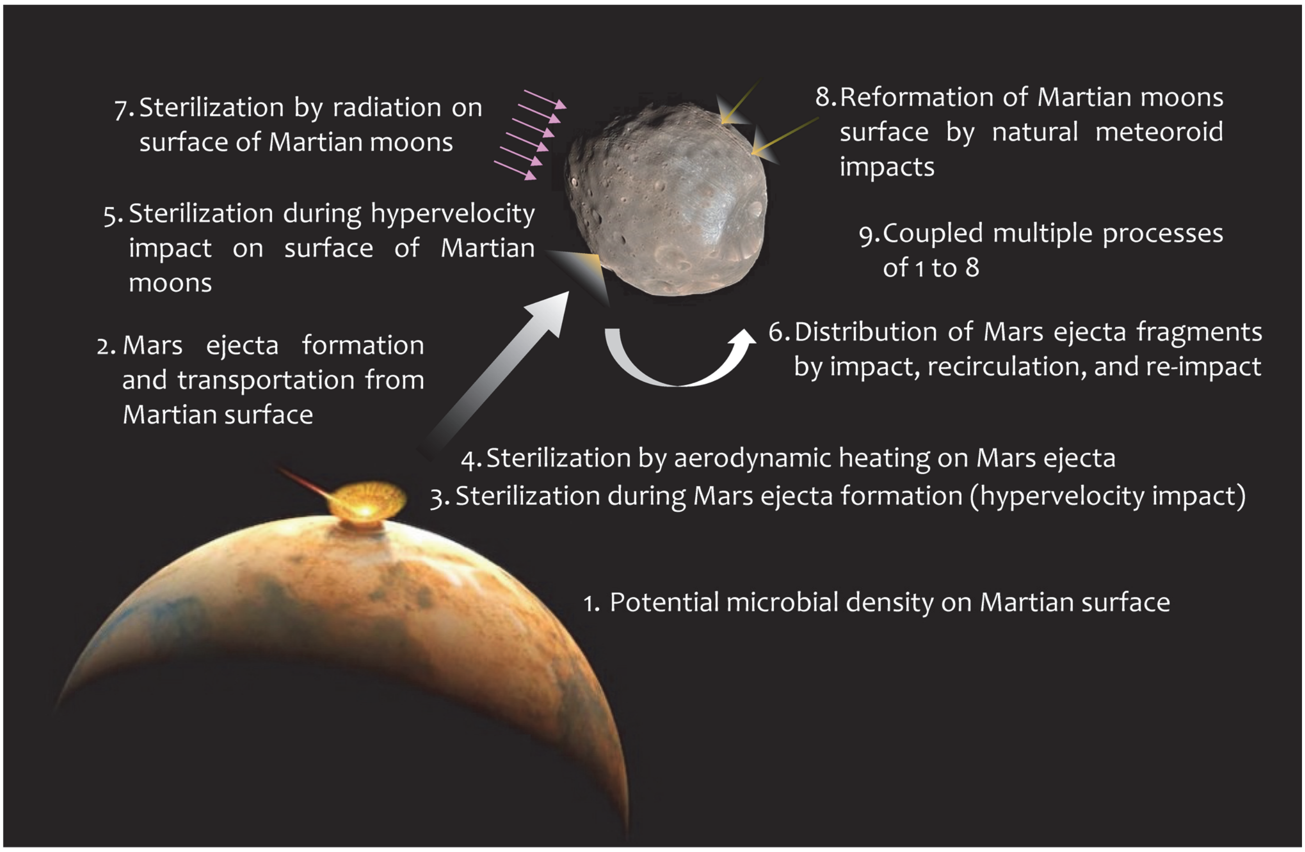

Fig. 2-1 Potential scenario of microbial contamination of Martian moons.

Microorganisms contained in the craters and in the thin layers on the surface of the Martian moons are expected to gradually decrease with time due to sterilization by solar and galactic cosmic radiation (7). However, it should be noted that, in addition to Mars ejecta, natural meteoroids continuously impact on the surface of the Martian moons as well, creating craters, scattering fragments, and eventually forming a thick layer of regolith around the craters on the surface of the Martian moons, as illustrated in Figs. 2-2c and 2-2d. Because of this continuous phenomenon, a certain portion of the contaminated surface can be immediately covered with a thick layer of regolith before sufficient sterilization has been completed by radiation, leaving protected areas where the microbial density decreases more slowly than in the exposed areas. Above all, the surface of the Martian moons can be roughly divided into three categories as illustrated in Fig. 2-2d:

1) Craters produced by Mars ejecta impacts, where microbial density may remain relatively high to a considerable depth for long, since radiation sterilization progresses slowly in deep regions.
2) Areas covered with thick regolith layers produced by natural meteoroid impacts, where microbial density decreases at a moderate speed by radiation sterilization.
3) Exposed common areas, where microbial density quickly decreases by radiation sterilization.

In the following part of this article, the processes described above are quantitatively examined to obtain an estimate of the potential microbial density on the surface of the Martian moons, from which microbial contamination probability in samples collected on the surface of the Martian moons is assessed.

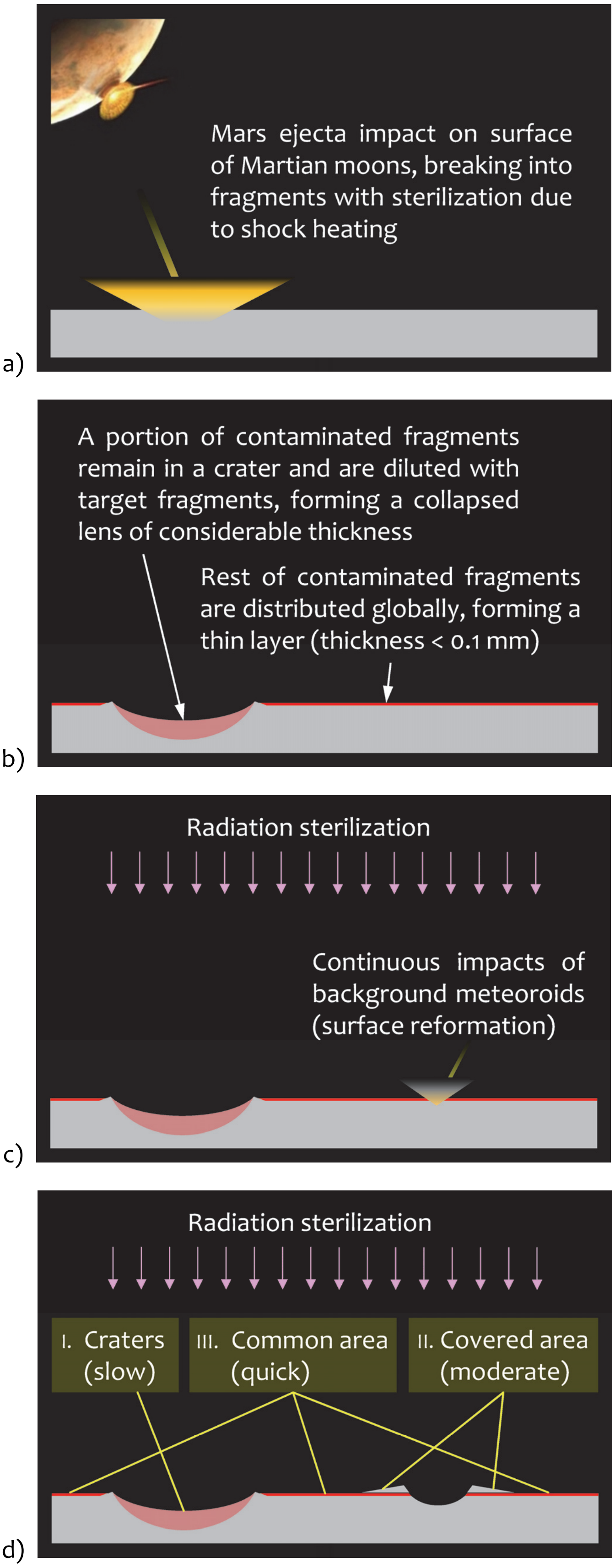

Mars ejecta impact on surface of Martian moons, breaking into fragments with sterilization due to shock heating

A portion of contaminated fragments remain in a crater and are diluted with target fragments, forming a collapsed lens of considerable thickness

Rest of contaminated fragments are distributed globally, forming a thin layer (thickness < 0.1 mm)

Continuous impacts of background meteoroids (surface reformation)

Fig. 2-2 Distribution of Mars ejecta fragment over the surface of Martian moons.

2.2. Comparison to SterLim Study

In Table 2-1, comparison is made between the physical processes taken into consideration and the numerical procedures used in the SterLim and this study. Potential microbial density on the Martian surface, which is assumed as that of the Atacama Desert in the SterLim study, is revised in this study by analogy from the terrestrial areas having the similar arid and cold environments to the Martian surface. Mars ejecta formation and transportation are based on the results of Melosh and Chappaz in the SterLim study (Melosh, 2011; Chappaz et al., 2013), while the 3-dimensional Smoothed Particle Hydrodynamics (SPH) computation for oblique impacts and associated trajectory analysis are newly conducted in this study. Sterilization during meteoroid impacts on the Martian surface, and sterilization by aerodynamic heating on Mars ejecta are newly taken into account in this study. Microbe survival rate during hypervelocity impacts of Mars ejecta against the Martian moons is assumed uniquely as 0.1 in the SterLim study, based on the impact experiments, since impact velocities are estimated below 2 km/s. Here, the hypervelocity impact sterilization model is renewed and extended to a higher velocity range by using the experimental data of the SterLim study, since the results of the SPH computation and the trajectory analysis suggest that impact velocities are in general higher than 2 km/s. Radiation sterilization model is taken from the SterLim study. The greatest difference in this study is that, in the SterLim study, Mars ejecta is assumed to be continuously and globally deposited on the surface of the Martian moons, whereas three-dimensional distribution of Mars ejecta fragments is considered, according to the most probable scenario of past meteoroid impact events on the Martian surface in the history of Mars.

Table 2-1 Comparison to SterLim Study

Elementary processes		SterLim	Present study
1	Potential microbial density on Martian surface	Assuming same microbial density as Atacama Desert	Similar to SterLim, but a slight acceptable correction introduced
2	Mars ejecta formation and transportation	Based on study of Melosh	SPH computations newly conducted for statistical analysis
3	Sterilization during Mars ejecta formation	No model introduced (microbe survival rate = 1)	Sterilization during meteoroid impact additionally introduced
4	Sterilization by aerodynamic heating on Mars ejecta	N/A	Thermal analysis of Mars ejecta conducted along trajectories
5	Sterilization during hyper-velocity impact on surface of Martian moons	Microbe survival rate ~ 0.1 for velocity <2 km/s, based on impact experiments	Impact sterilization model renewed. SPH and trajectory analysis suggesting more frequent sterilization going on
6	Distribution of Mars ejecta fragments by impact, recirculation, and re-impact	Homogeneous deposition by averaging the incoming flux	Crater formation by Mars ejecta with retention & scattering of Mars ejecta fragments taken into account
7	Sterilization by radiation on Phobos surface	Sterilization model based on experimental fact	Same as SterLim, but integration in depth direction newly conducted
8	Surface reformation by natural meteoroid impacts	N/A	Continuous natural meteoroid impacts on Martian moons taken into account
9	Coupled multiple processes of 1 to 8[]	N/A	Statistical analysis of microbial contamination conducted

3. Potential Microbial Density on Martian Surface

Navarro-González et al. (2003) reported microbial densities ranging from 10^5 to 10^{10} CFU/kg in the Atacama Desert, as shown in Fig. 3-1. However, it should be noted that microbial densities measured in the Yungay area, which is the most arid zone in the Atacama Desert, are not greater than 10^7 CFU/kg. Maier et al. (2004) reported microbial densities ranging from 10^6 to 10^8 CFU/kg in the Yungay area as well. Their results show good agreement with those of Navarro-González et al. (2003). Since the Martian surface is in general extremely arid as the Yungay area, it might be reasonable to take the values measured in this area.

Glavin et al. (2004) estimated bacterial cell abundances near the Yungay area, finding that bacterial counts for the surface and subsurface samples of 0.7×10^9 cells/kg and 9.6×10^9 cells/kg, respectively, by using the DAPI (4,6-diamidino-2-phenylindole) staining method. More recently, Drees et al. (2006) measured culturable biomass count of 5.40×10^6 CFU/kg in the Yungay area, and 9.11×10^7 to 1.36×10^8 CFU/kg in the surrounding area. Phospholipid fatty acids (PLFA) analysis of Lester et al. (2007) indicated 8.5×10^9 to 6.0×10^{10} cell equivalents/kg in the Yungay area, while culturing of soil extracts on R2A and TSA media yielded 6.3×10^5 to 5.2×10^6 CFU/kg at the same time. Connon et al. (2007) reported that PLFA concentrations ranged from 2×10^8 to 7×10^9 cell equivalents/kg while R2A culturing yielded 4.7×10^4 CFU/kg in the Yungay area. It should be noted that the cell equivalent includes inactivated microbe cells, so that they are much greater than the culturable biomass count. Above all, microbial density in the hyperarid environments is considered to range from 10^6 to 10^8 CFU/kg, or 10^8 to 10^{10} cells/kg for conservative estimation.

In addition to the Atacama Desert, microbial populations in Antarctic permafrost are considered to give closer information, since the Antarctic permafrost is more likely to bear analogy with the Martian environments due to low temperature. Aislabiea et al. (2006) reported that the total direct count by molecular analysis ranged from 10^9 to 1.3×10^{11} cell equivalents/kg, while number of culturable heterotrophs was found to

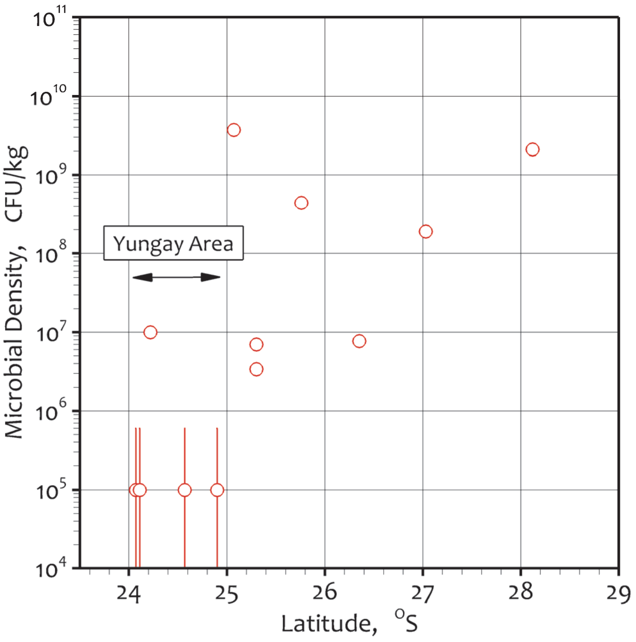

Fig. 3-1 Microbial density measured in the Atacama Desert (Navarro-González et al., 2003).

range from 10^4 to 3.8×10^8 CFU/kg, depending on the environments. It should be noted that cell count was the lowest or below the detection limit of 10^4 CFU/kg in the coldest areas, which are Venda and Mt. Fleming in their study. Gilichinsky et al. (2008) measured the number of bacterial cells in the frozen ground and the buried soils of Antarctica, finding that the total cell number counted by epifluorescence microscopy was 10^8–10^9 cells/kg. Very recently, Goordial et al. (2016) reported very low microbial biomass of $1.4\text{-}5.7\times10^6$ cells/kg in both the dry and ice-cemented permafrost of the University Valley, which is one of the coldest and driest regions in the McMurdo Dry Valleys (MDVs) of Antarctica, by using Dichlorotriazinyl Aminofluorescein (DTAF) stain. 2 orders of magnitude higher cell counts ($1.2\text{-}4.5\times10^8$ cells/kg) were detected in the active layer and permafrost soils from the Antarctic Peninsula, which has more moderate environments than the University Valley. The above results indicate that microbial density in Antarctica is at the same order as that in the Atacama Desert or lower because of extremely low temperature. This suggests that microbial density on Mars may be lower than that of the Atacama desert because of much lower temperature, though hyperarid conditions are common to both.

There is no additional scientific evidence obtained so far to determine microbial density on Martian surface. This means that the baseline value for microbial density on the Martian surface is of political nature rather than of scientific at this moment. We may have a lot of knowledge gaps on this problem. From the above discussion, it would be reasonable to assume that the baseline value or microbial density on the Martian surface is between 10^6 to 10^8 CFU/kg. In the following part of this article, we use the maximum value of 10^8 CFU/kg on the Martian surface for conservative assessment, although we consider the value of 10^{10} CFU/kg on the Martian surface just in case in Section 10.

4. Sterilization during Mars Ejecta Formation

Mars ejecta transported to the Martian moons are produced by hypervelocity impacts of meteoroids against the Martian surface. In such the impact events that can transport the ejected rocklets to the Martian moons, the incident meteoroids must have considerably high impact velocities, since the ejected rocklets should have velocities higher than 3.8 km/s at departure from the Martian surface to reach the Phobos orbit. Because of hypervelocity impacts, when the surface on which a meteoroid impacts is sufficiently rigid, considerable shock-heating must occur in fragmentation of the impactor and the target surface, as reported by Kurosawa and Genda (2018), resulting in high sterilization of Mars ejecta. Such the heat source due to plastic deformation of the pressure-strengthened rocks has been overlooked for a long time (Melosh and Ivanov, 2018). In order to confirm this, shock-heating generated among ejecta is numerically simulated by using the iSALE code (Amsden et al., 1980; Ivanov et al., 1997; Wünnemann et al., 2006) with taking internal friction and plastic deformation into consideration. Strength parameters are taken from the work of Ivanov et al. for basalt (Ivanov et al., 2010). The results are shown in Fig. 4-1b and compared to the results without internal friction and plastic deformation shown in Fig. 4-1a.

In Fig. 4-1, symbols represent the ejected particles produced in a vertical impact with an impact velocity at 3.5 km/s. The impact velocity corresponds to the normal component of the impact velocity for at 45-degrees-obluque impacts at the escape velocity of Mars. Thus, the figure shows a minimum estimate of the degree of shock heating. Color of symbols represent the ejection velocity, and the area surrounded by a sold curve

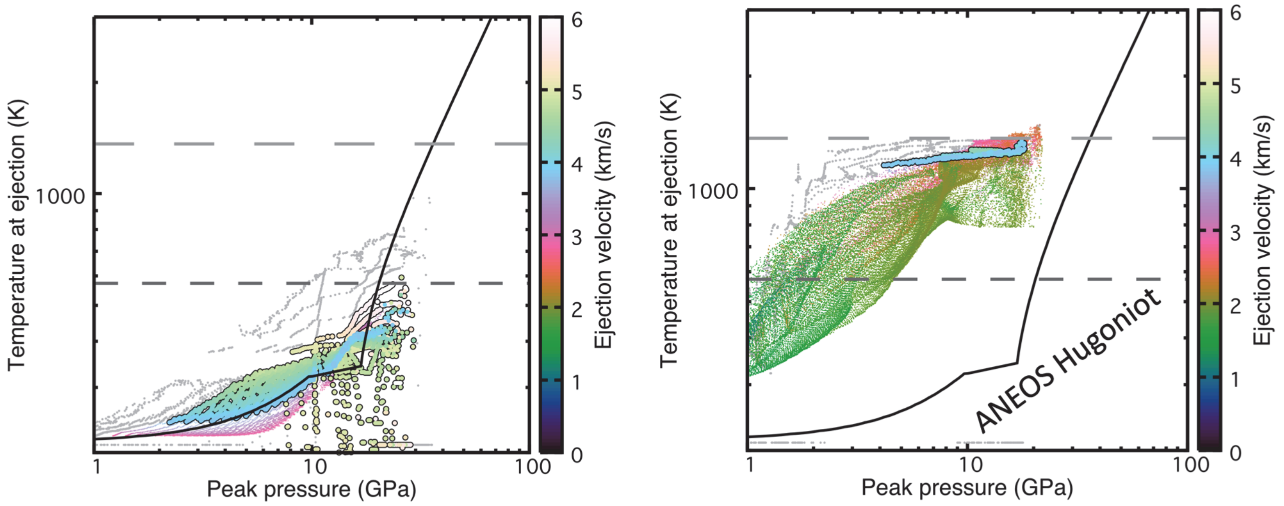

a)

b)

Fig. 4-1 Temperature of ejected particles at ejection in a hypervelocity impact in relation to ejection velocity; a) without internal friction and plastic deformation, and b) with internal friction and plastic deformation (Kurosawa and Genda, 2018). The two grey dashed lines indicate the temperatures required for the melting of basaltic rocks (upper) and sufficient sterilization (lower).

represents the particles having velocities higher than 3.8 km/s, which is the minimum velocity to reach the Phobos orbit. It is seen that a considerable portion of ejecta do not undergo shock-heating, remaining their temperature below 300°C (denoted by the lower dashed line in Fig. 4-1) when internal friction and plastic deformation are not present (Fig. 4a). In contrast to this, the ejecta having velocities greater than 3.8 km/s are heated above 1,000 K when the internal friction and plastic deformation is taken into account (Fig. 4-1b). This suggests that the Mars ejecta reaching the Phobos orbit and beyond cannot avoid shock-heating when the target ground is sufficiently rigid. According to the heat test results in the SterLim study, the microbial survival rate (N/N_0 where N_0 is the initial number of microbes) is less than 10^{-2} for temperatures above 300°C. These facts suggest that microbial survival rate during Mars ejecta formation may be much less than 10^{-2} when the target surface is sufficiently rigid. This must be common for the aged surfaces on Mars.

Park et al. (2008) reported an apparent evidence of sufficient shock heating in Dhofar 378. This fact supports the above argument that the microbial survival rate is sufficiently small in Mars ejecta formation. At the same time, however, Nyquist et al. (2001) reported that a considerable portion of Martian meteorites do not have a sign of shock-heating. This might come from the fact that the geochemical barometers, such as shock melted glasses (e.g., Fritz et al., 2017) and atomic diffusion (e.g., Takenouchi et al., 2017), for the estimation of the temperature rise have relatively low sensitivities at a moderate temperature (several hundred K). Nevertheless, the results by Nyquist et al. (2001) suggest that the Mars ejecta can be sometimes accelerated to the escape velocity and above without sufficient shock-heating. Further studies may be needed on shock-heating and the attainable maximum temperature during Mars ejecta formation. At this moment, the microbial survival rate = 0.1 in Mars ejecta formation is considered to be a good assumption. This assumption seems to be too conservative for the rigid Martian surface material, and reasonable for non-rigid Martian surface material, based on the results of numerical analysis shown in Fig. 4-1, which may be consistent with the facts of Martian meteorites as well.

5. Sterilization by Aerodynamic Heating

Mars ejecta produced by hypervelocity impacts on the Martian surface must undergo aerodynamic deceleration and consequent aerodynamic heating along their flight trajectory in Martian atmosphere. From an orbital mechanics viewpoint, Mars ejecta need to have at least an initial ejection velocity higher than 3.8 km/s to reach the orbits of the Martian moons. The higher the initial ejection velocity, the greater the aerodynamic heating they receive. For Mars ejecta having small diameters, aerodynamic deceleration and aerodynamic heating become remarkable. In order to examine the effect of aerodynamic heating on Mars ejecta ascending to the Martina moons, trajectory calculations under the influence of the Martian atmosphere, Computational Fluid Dynamic (CFD) computations around Mars ejecta in hypersonic flight, and heat transfer analysis of Mars ejecta are conducted in this study.

5.1. Numerical Approaches

For the purpose of this analysis, a Mars atmosphere model, which is shown in Fig. 5-1, has been developed by using Mars-Global Reference Atmospheric Model 2005 (Mars-GRAM 2005 v1.3) (Duvall et al., 2005; Justus et al., 2005), as a global and annual average of the Martian atmosphere in 2000. At first, a representative aerodynamic drag coefficient and a distribution of aerodynamic heat transfer rate around Mars ejecta are estimated by CFD calculations. In this analysis, Mars ejecta are assumed to be in a spherical form, having diameters ranging from

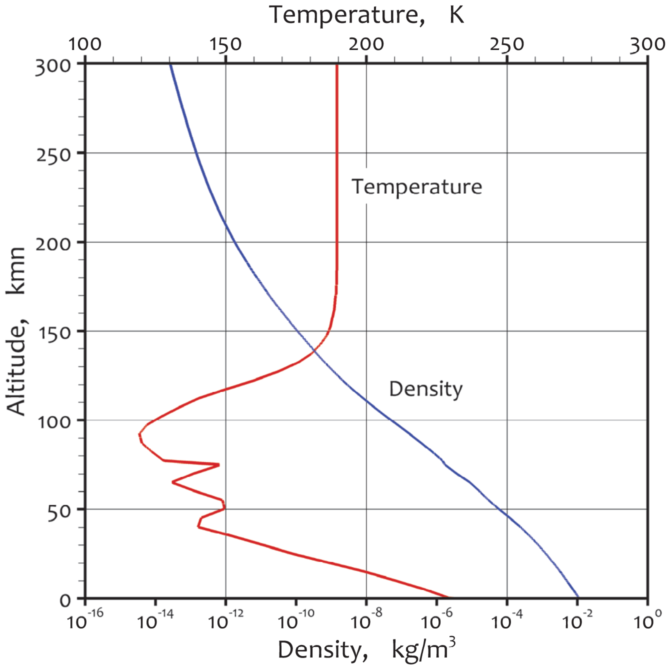

Fig. 5-1 Mars atmosphere model developed by using Mars-GRAM 2005 v1.3 (Duvall et al., 2005; Justus et al., 2005).

0.02 to 10 m. Atmospheric temperature and pressure are assumed as 210 K and 0.8 kPa, respectively, which are the values at an altitude of 0 m in the Mars atmosphere model. The Mars atmosphere composition is assumed as 95% CO_2 and 5% N_2. JAXA Optimized Nonequilibrium Aerothermodynamic Analysis (JONATHAN) code (Fujita et al., 2006), which a compressible flow solver with chemical reactions among high-temperature gases incorporated, is used to compute an aerodynamic drag coefficient and a distribution of aerodynamic heat transfer rate for Mars ejecta.

Secondly, based on the aerodynamic drag coefficient obtained above, orbital dynamics of Mars ejecta in the Martian atmosphere is numerically simulated by changing initial ejection angles and velocities of Mars ejecta, to obtain the threshold initial ejection velocity required for Mars ejecta to reach the Phobos orbit (evolution radius = 9,376 km) for each initial ejection angle and diameter of Mars ejecta. In this analysis, a trajectory analysis code used in the preceding study (Fujita et al., 2012) is used. Time history of aerodynamic heat transfer rate at the forebody stagnation point is determined by Tauber's formula (Tauber et al., 1990; Tauber et al., 1991) along the flight trajectory. Distributions of aerodynamic heat transfer rate around Mars ejecta are then estimated by using the representative distribution obtained by the CFD analysis.

According to time history of aerodynamic heat transfer rate distributions around Mars ejecta, unsteady heat conduction analysis about Mars ejecta is conducted to obtain evolution of temperature distribution inside Mars ejecta, with taking radiation cooling on the surface into account. In this analysis, Mars ejecta are assumed as homogeneous basalt having density of 2.8 Mg/m^3, specific heat of 2.8 Mg/m^3, thermal conductivity of 2.3 W/m·K, and emissivity of 0.95. The initial temperature of Mars ejecta is assumed as 210 K, which is identical with the atmospheric temperature on the Martian surface. Finally, according to evolution of internal temperature distributions, microbial survival rate is deduced as a function of the initial ejection angle and the diameter of Mars ejecta.

5.2. Numerical Results

Distributions of gas temperature and flow streamlines obtained by CFD analysis are presented in Fig. 5-2 for representative diameters, 0.1 and 10 m. It is seen that gas temperature around Mars ejecta is higher than 1,000 K, suggesting that microbes on the surface are quickly annihilated completely. Gas temperature distribution hardly depends on diameter of Mars ejecta. Distributions of heat transfer rate around Mars ejecta are given in Fig. 5-3. As a diameter of Mars ejecta increases, the heat transfer rate decreases accordingly. Because of a well-known numerical instability which is inevitable in the axisymmetric analysis, there are some errors in heat transfer rate around the forebody stagnation point. In order to avoid such errors, a fitting function is given to reproduce distribution of the heat transfer rate, as denoted by a solid curve in Fig. 5-3. The fitting function is used to determine evolution of the heat transfer rate distribution around Mars ejecta from evolution of the heat transfer rate at the stagnation point, which is obtained by trajectory analysis. For conservative analysis of heat conduction, heat transfer to the aftbody region is neglected in the fitting function, as shown in Fig. 5-3.

The results of trajectory analysis are summarized in Figs. 5-4 and 5-5, in terms of the threshold velocity to reach the Phobos orbit and the corresponding total heat transferred to the stagnation point for Mars ejecta reaching the Phobos orbit, as a function of the ejection angle and the diameter (it should be noted that the ejection angle is denoted as the flight path angle in the figures). The threshold initial velocity becomes high as the ejection angle decreases and as the diameter decreases. This is because Mars ejecta are more decelerated by aerodynamic drag due to increase in flight path length through the Martian atmosphere as the ejection angle decreases. Since the aerodynamic drag force is proportional to the square of the diameter, Mars ejecta having small diameters are more likely to be decelerated than those having large diameters. As a result, Mars ejecta having diameters smaller than 0.1 m are difficult to leave the Martian atmosphere. The total heat transferred to the stagnation point of Mars ejecta becomes significantly high as the ejection angle decreases and as the

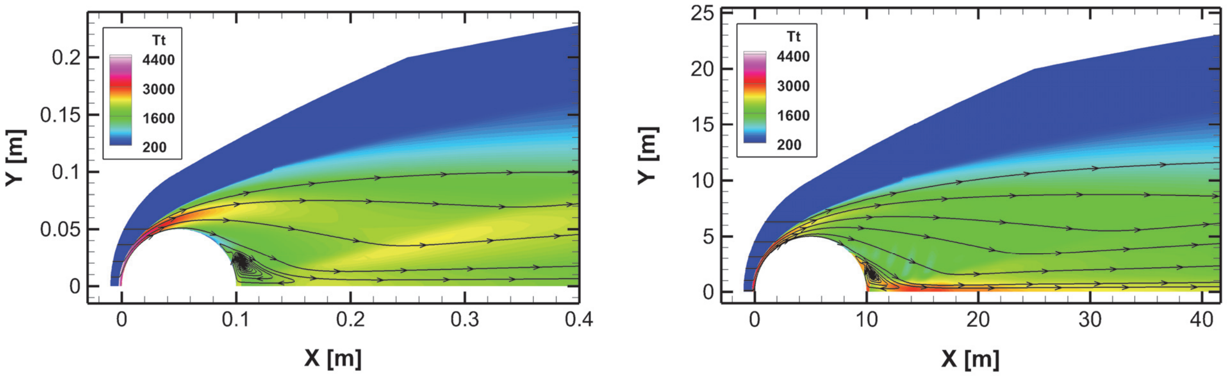

a) b)

Fig. 5-2 Distributions of gas temperature and flow streamlines around Mars ejecta obtained by JONATHAN; a) diameter = 0.1 m and b) 10.0 m.

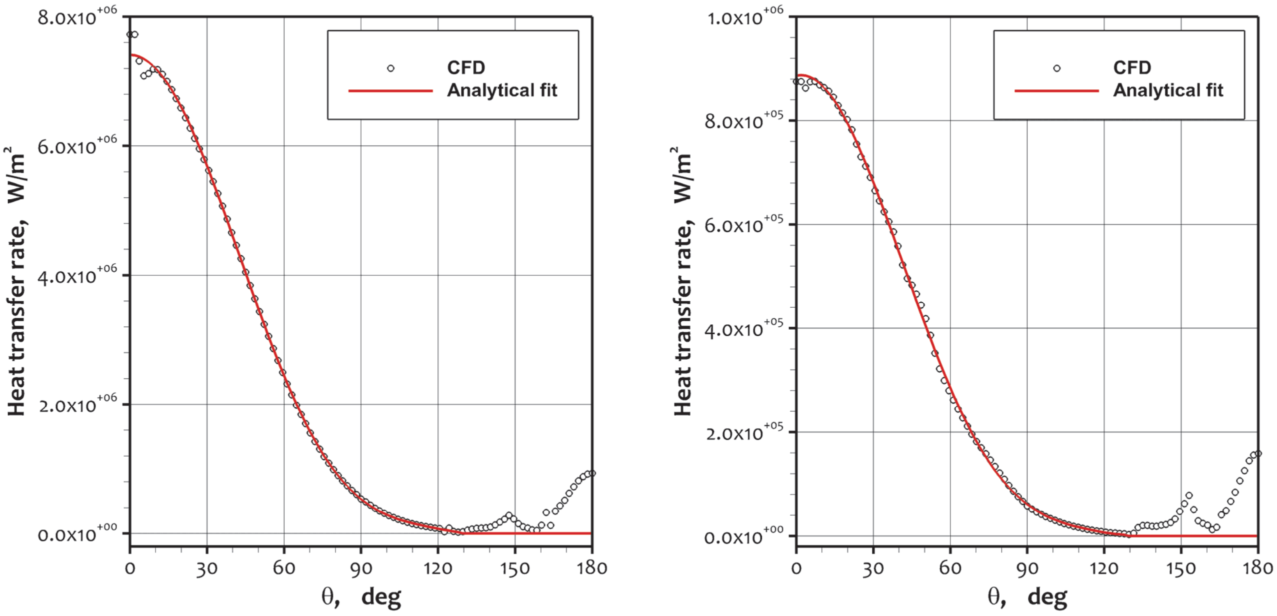

a) b)

Fig. 5-3 Distributions of heat transfer rate around Mars ejecta obtained by JONATHAN; a) radius = 0.1 m and b) 10.0 m.

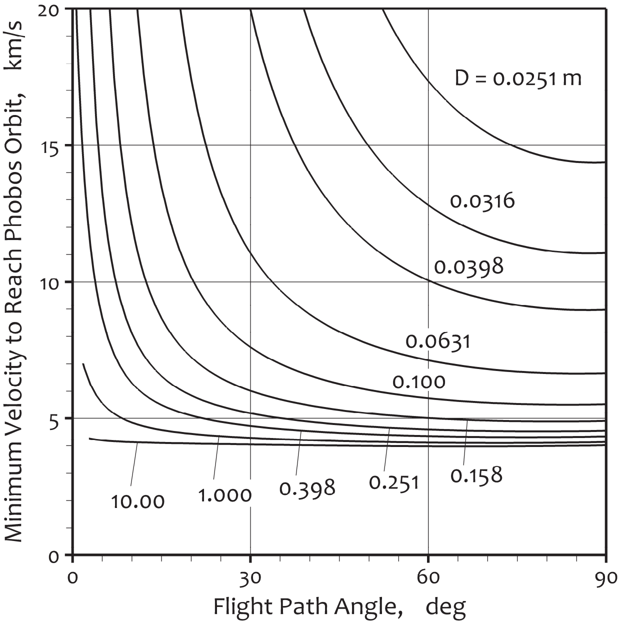

Fig. 5-4 Threshold initial velocity of Mars ejecta to reach Phobos orbit for different ejection angles and diameters.

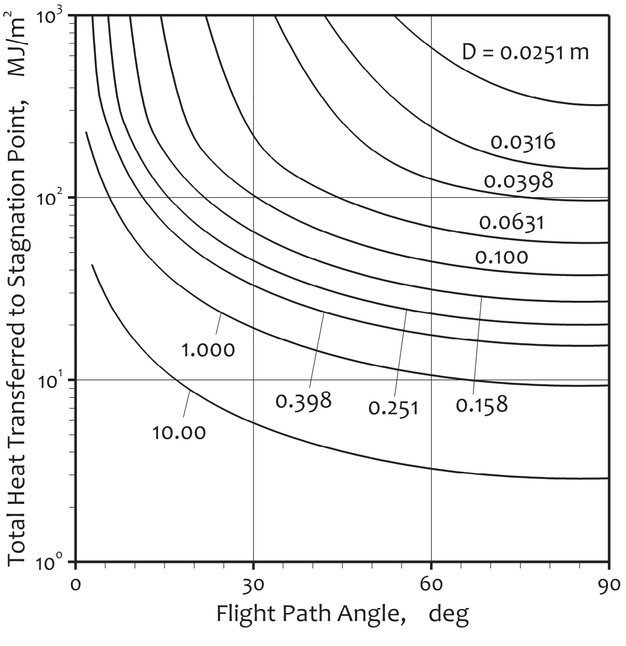

Fig. 5-5 Total heat transferred to stagnation point of Mars ejecta for different ejection angles and diameters.

diameter decreases. This is because the initial velocity has to be increased as described above, and because the stagnation-point heat transfer rate essentially increases as the radius of local curvature decreases (e.g. Tauber et al., 1991). More detailed analysis on thermal behavior of Mars ejecta is given in the next section.

5.3. Internal Temperature of Mars Ejecta

According the results obtained by CFD and trajectory calculations, time history of the aerodynamic heat transfer distribution around Mars ejecta is obtained. Using this as the boundary condition, an unsteady differential equation of heat conduction in a 2-D axisymmetric form is integrated with respect to time by the 4th order Runge-Kutta method. Evolution of internal temperature distribution so obtained is illustrated in Fig. 5-6 as a representative example. In this case, since aerodynamic heating is completed within several ten seconds from ejection, the region with the highest temperature is located near the surface in Fig. 5-6a, then gradually diffuses to the whole sphere over time. The maximum temperature encountered at each internal location during the period from ejection to arrival at the Phobos orbit is shown in Fig. 5-7 for the representative diameters of Mars ejecta. It is seen that, as the diameter decreases, a portion of the region that encounters temperature above 500°C quickly increases, and the maximum temperature becomes higher.

5.4. Microbial Survival Rate for Aerodynamic Heating

Finally, microbial survival rates for aerodynamic heating are estimated from the maximum internal temperature obtained above, with an assumption that microbes are completely annihilated if temperature is maintained above 500°C for more than 0.5 sec. The results are summarized in Table 5-1. It is seen that a considerable portion of microbes are expected to be annihilated for Mars ejecta with a 0.02-m diameter, while they are hardly sterilized for diameters as large as 0.1 m and above. As already described above, Mars ejecta having diameters less than 0.1 m are difficult to reach the Phobos orbit due to aerodynamic deceleration (see Sec. 5.2). Above all, it is concluded that most of Mars ejecta transported to the Martian moons have diameters as large as 0.1 m and more, and are hardly sterilized except for their surfaces. Those whose diameter is smaller than 0.1 m hardly reach the Martian moons, and are considerably sterilized even if they arrive.

Table 5-1 Microbial survival rate for aerodynamic heating.

Diameter [m]	Flight path angle [deg]			
	90°	75°	60°	45°
0.0200	0.138	0.123	0.067	0.000
0.0251	0.323	0.310	0.266	0.190
0.0316	0.494	0.481	0.431	0.341
0.0398	0.632	0.625	0.590	0.507
0.0631	0.806	0.803	0.785	0.748
0.100	0.899	0.897	0.888	0.867
0.398	0.987	0.987	0.986	0.983
1.000	0.997	0.997	0.997	0.996

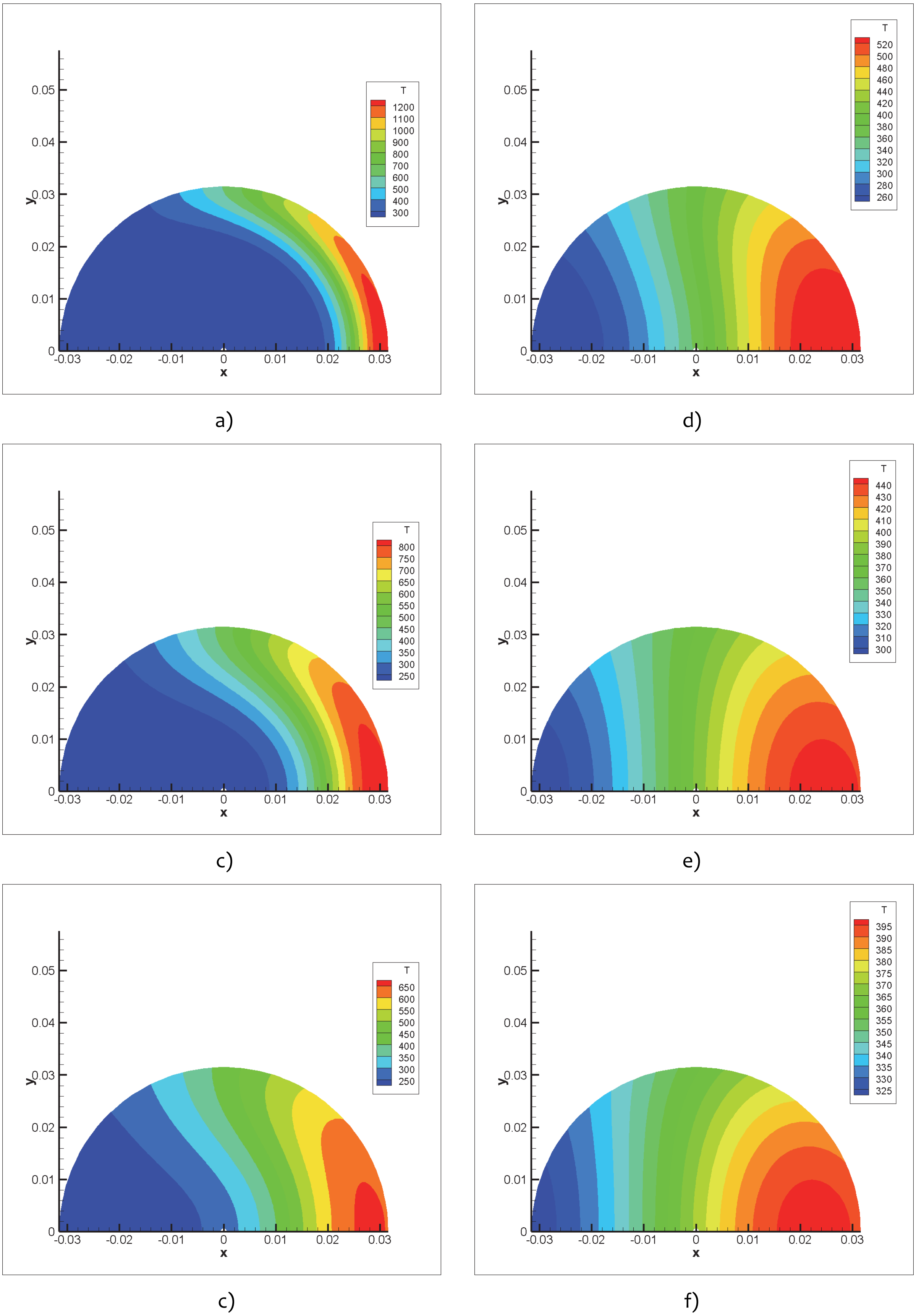

a) d)

c) e)

c) f)

Fig. 5-6 Evolution of internal temperature of Mars ejecta with diameter = 0.0631 m and ejection angle = 90°; a) t = 20 sec., b) 50 sec., c) 100 sec., d) 200 sec., e) 400 sec., and f) 600 sec.

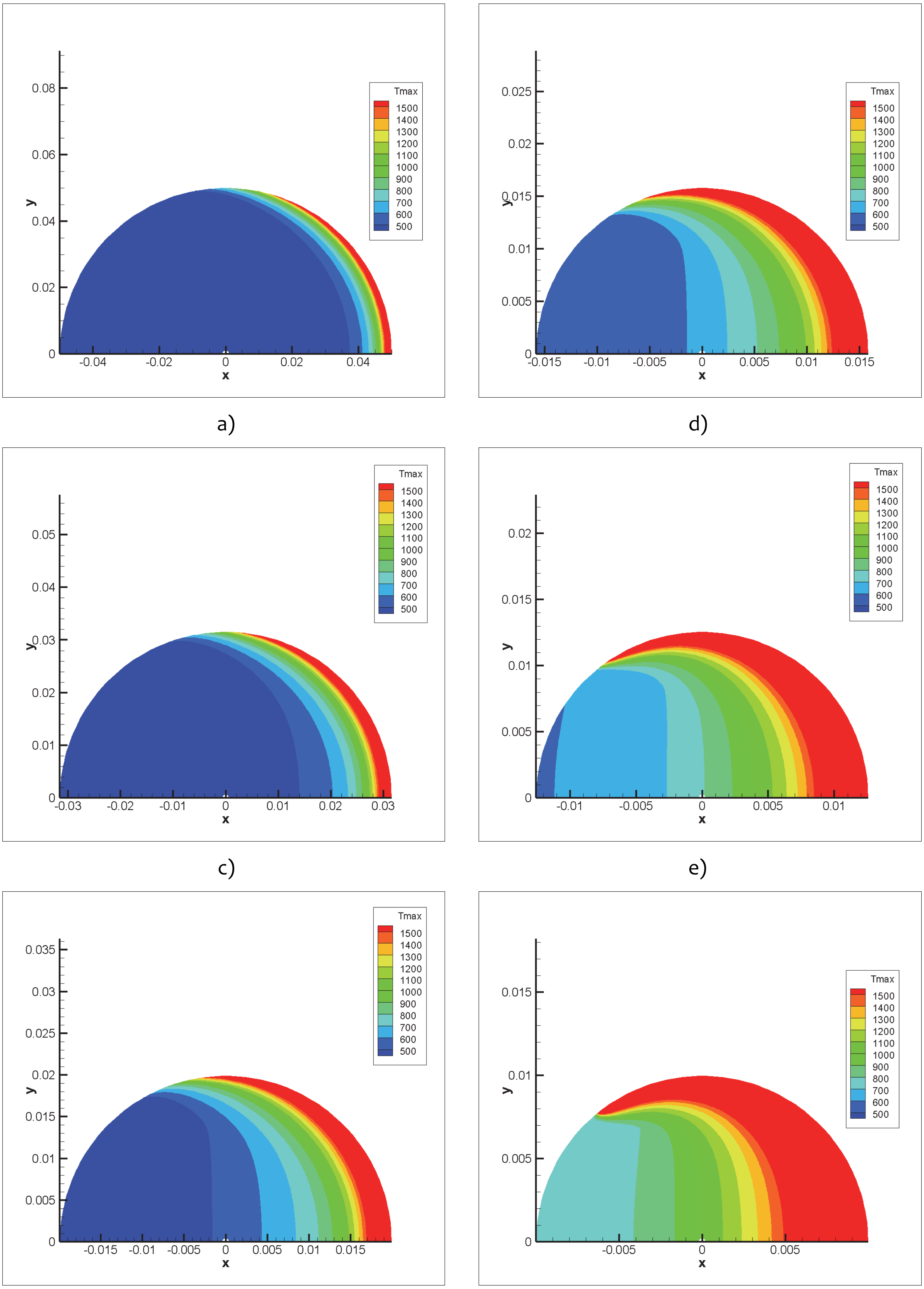

a) d)

c) e)

c) f)

Fig. 5-7 Maximum internal temperature of Mars ejecta with ejection angle = 90°; a) diameter = 0.1 m, b) 0.0631 m, c) 0.0398 m, d) 0.0316 m, e) 0.0251 m, and f) 0.0200 m.

6. Impact Sterilization on Surface of Martian Moons

6.1. Shock-Heating

Mars ejecta arriving at the Martian moons undergo hypervelocity impacts against the surface of the Martian moons, just as meteoroids impact on the Martian surface in Mars ejecta formation. Because of a high energy impact associated with shock-heating of an impacting object as well as indigenous materials on the surface, considerable impact sterilization of microbes in Mars ejecta is expected. However, there are two essential differences between the hypervelocity impacts on the surface of Mars and the Martian moons. At first, impact velocities are expected to be higher in Mars ejecta formation on the Martian surface, since produced Mars ejecta should have initial velocities higher than 3.8 km/s to reach the Phobos orbit. Secondly, on the surface of the Martian moons, microbes are only contained in Mars ejecta which undergo hypervelocity impacts and are totally crashed into fragments with shock-heating, while on the Martian surface, microbes are globally distributed in the materials on the Martian surface, which are scattered by hypervelocity impacts as Mars ejecta. Because of these differences, the microbial survival rate for hypervelocity impacts on the surface of the Martian moons should be determined in a different manner from that for Mars ejecta formation (Section 4).

In hypervelocity impacts of Mars ejecta on the surface of the Martian surface, since Mars ejecta as incident objects essentially have high kinetic energy, considerable shock-heating must occur among incident materials on impact, while heat transfer to target materials is not so efficient as shown in the SterLim study. In order to examine the efficiency of shock-heating among incident materials, temperature rise among incident materials is numerically assessed by using the same way performed in Section 4 except that we focused on the degree of shock heating in the projectile. Strength parameters are taken from Ivanov et al. for basalt (Ivanov et al., 2010). Typical results are shown in Fig. 6-1. As the impact velocity increases, impact shock-heating is seen to become more significant among incident materials. This suggests that impact sterilization among incident materials becomes enhanced with increasing impact velocity.

It must be physically true that microbial survival rate decreases as impact velocity increases, since kinetic energy transferred to shock-heating increases accordingly. Such a trend is clearly seen among the impact test results of the SterLim study as well (Fig. 6-2). However, in the SterLim study, the microbial survival rate is assumed to be uniquely 0.1 regardless of impact velocity. This is because impact velocities of Mars ejecta are considered in the SterLim study to be lower than 2 km/s in average. However, the SPH computation associated with trajectory analysis conducted in this study predicts that a major portion of Martian ejecta have impact velocities higher than 2 km/s, as described in Sec. 8. This suggests that Mars ejecta must be sterilized more efficiently than predicted in SterLim study. For this reason, an impact sterilization model is reproduced below so that it can apply to a higher velocity range above 2 km/s, based on the experimental data the SterLim study. It is strongly recommended to conduct additional impact tests with projectile velocities beyond 2 km/s.

6.2. Improved Model for Impact Sterilization

Microbial survival rate for hypervelocity impacts of Mars ejecta on the surface of the Martian moons can be reasonably defined by

$$N/N_0 = \exp(-CV^{\alpha}) \tag{6-1}$$

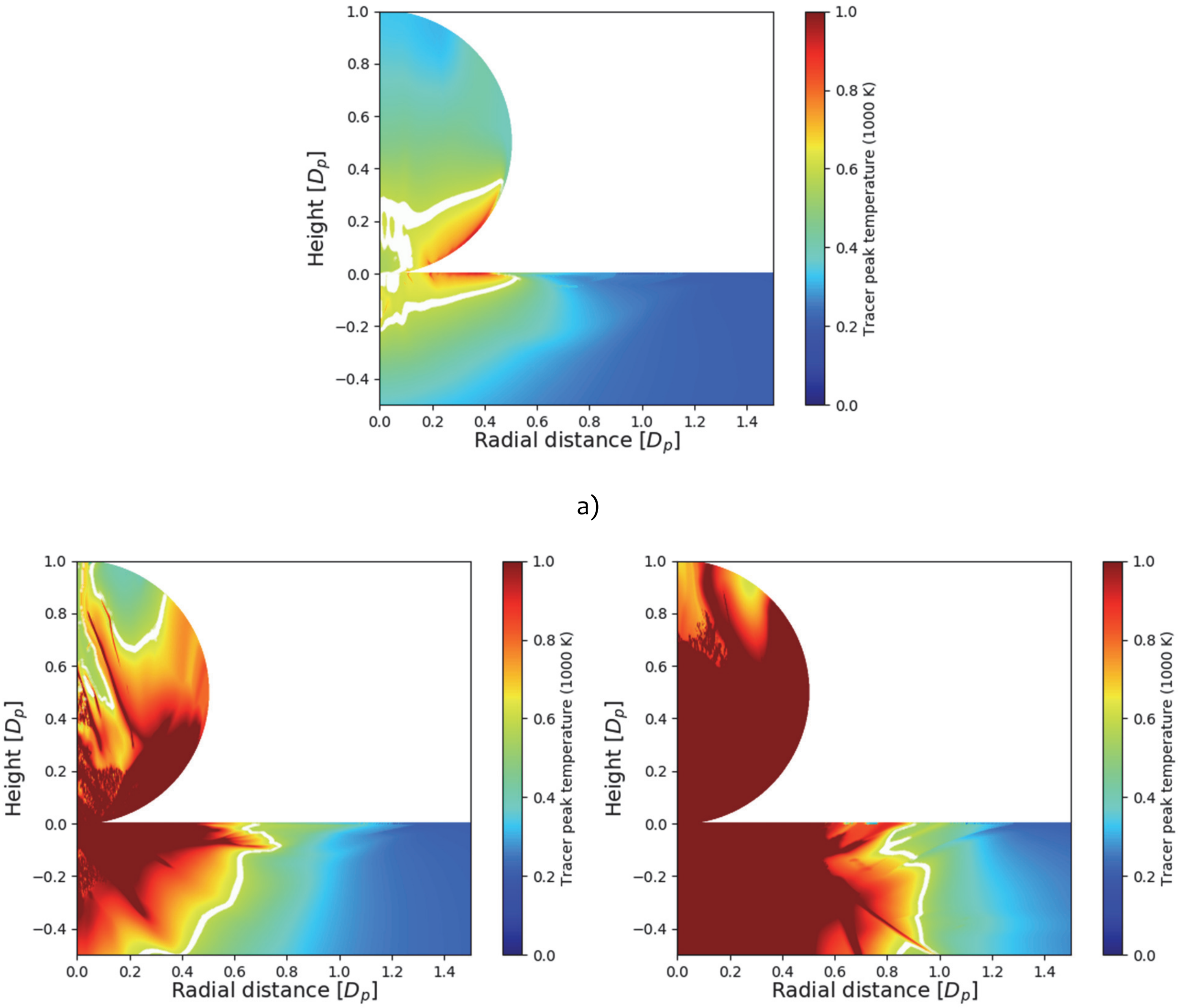

a)

b)

c)

Fig. 6-1 Temperature distribution in an incident particle and a target ground at scaled time of $t/t_s = 10$ in a hypervelocity impact with an impact angle of 90°; a) impact velocity = 1 km/s, b) 2 km/s, and c) 4 km/s (Kurosawa and Genda, 2018).

Where N and N_0 are the final and initial number of microbes, V is the impact velocity of a Mars ejecta, and C and α are the parameters to be adjusted. The above definition must be physically acceptable since kinetic energy of the incident object per unit mass is proportional to V^2, and so is the temperature increase in fragments after the impact. If transfer from kinetic to thermal energy is ideal, $\alpha = 2$ applies. Actually, some portion of the kinetic energy may be transferred to plastic deformation and shock-heating of the target materials, dissipating without transfer to shock-heating of the incident materials. For these reasons, α is not greater than 2 but close to 2.

The adjusting parameters are determined so that the impact test data of the SterLim study can be satisfactorily reproduced. There can be several fitting approaches, since the data are widespread in the tested velocity range, as shown in Fig. 6-2. The final form of microbial survival rate obtained in this study is given by

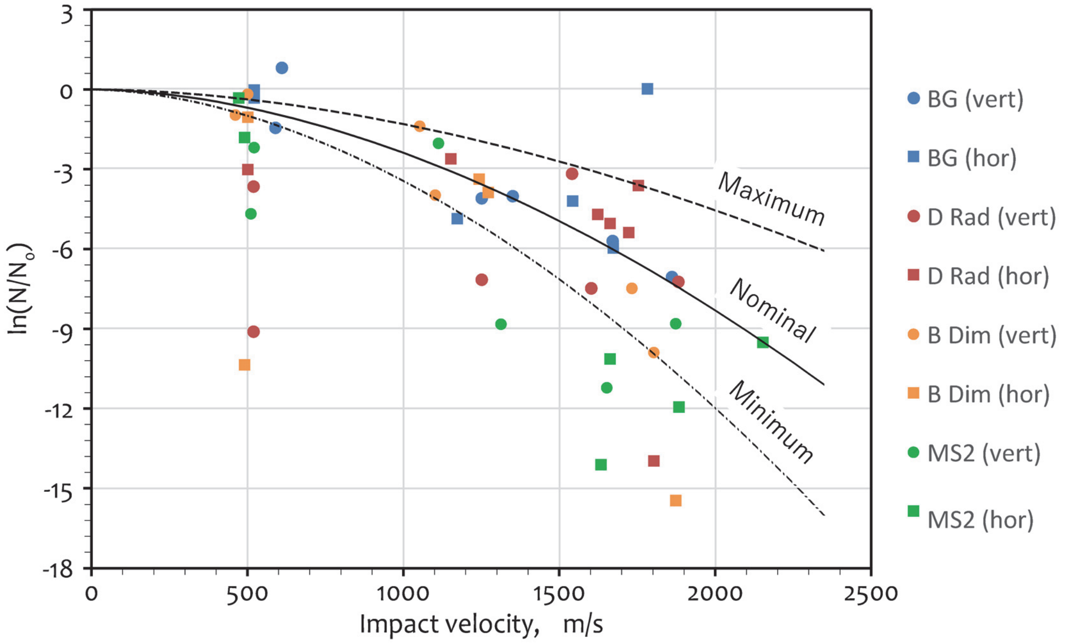

Fig. 6-2 Microbial survival rate for hypervelocity impacts of Mars ejecta on the surface of the Martian moons. The proposed model results are shown as black lines along with the impact tests results by SterLim study.

$$N/N_0 = \exp\left[-(9.5 \pm 4.3)\times10^{-6}\, V^{1.8}\right], \qquad (6\text{-}2)$$

where $C = 9.5\times10^{-6}$ is the nominal case, and each error corresponds to the maximum and the minimum cases in Fig. 6-2. The reproduced microbial survival rate is compared to the impact test data of the SterLim study in Fig.6-2. It is clear that verification of model accuracy is not sufficient for impact velocities above 2.0 km/s. It is strongly recommended to conduct additional impact tests in the higher velocity range for verification.

7. Radiation Sterilization

Microorganisms transported to the Martian moons are expected to be sterilized with time by solar and galactic cosmic radiation (γ-rays, proton, and α particles). Since the SterLim study offers excellent comprehensive data of radiation sterilization based on the thorough irradiation inactivation tests (Patel et al., 2017), these data are incorporated in this study without modification. The time constant (TC), which is the time needed to sterilize microorganisms by 1/e, is taken from the SterLim study (Summers, 2017), as shown in Fig. 7. For conservative assessment, TC for MS2 coliphage is used in this study. The microbial survival rate is calculated by

$$\frac{N}{N_0} = \exp\left(-\frac{t}{TC}\right) \qquad (7\text{-}1)$$

Where N_0 and N are the microbial density at the beginning and after the time t, and t is time in years.

TC is summarized in Table 7-1 for representative depth from the surface of the Martian moons. Microbial survival rate for representative time of interest is also shown in Table 7-1. It is seen that, as time increases and depth decreases, microbial survival rate quickly decreases. Since samples of the Martian moons

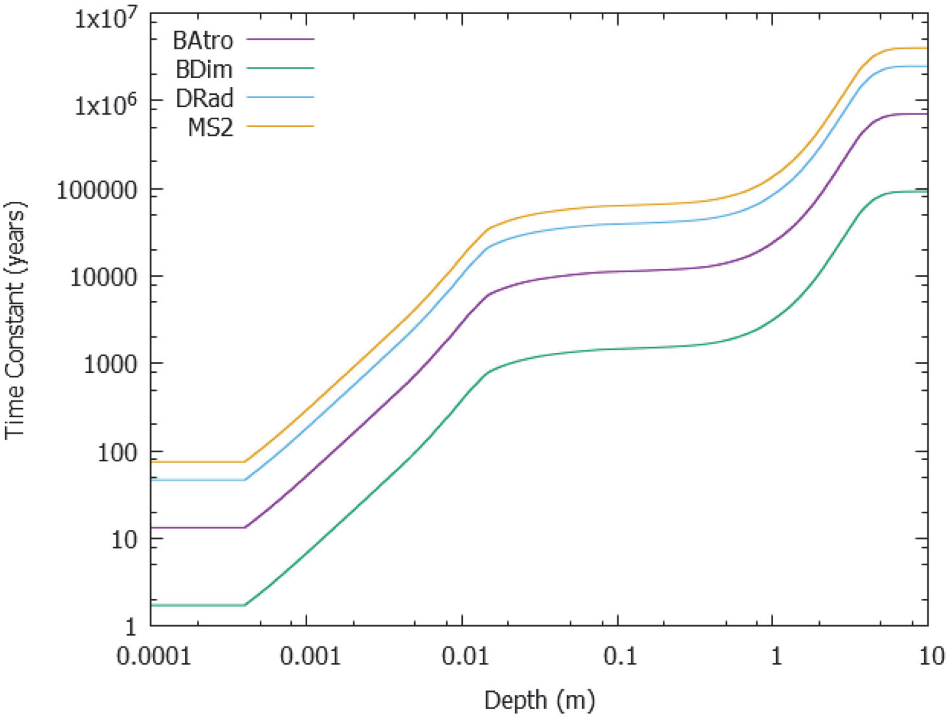

Fig. 7-1 Time Constant for radiation sterilization as a function of depth (Summers, 2017).

will be collected in a boring approach, it is more convenient to calculate the microbial survival rate averaged for the specific depth by integrating the microbial survival rate in the depth direction and dividing by depth. The averaged microbial survival rate so determined is summarized in Table 7-2. In general, the averaged microbial survival rate is smaller than the local survival rate at each depth, because microbial density decreases toward the exposed surface. From the results summarized in Table 7-2, it should be noted that microorganisms are expected to be annihilated by 3.9×10^{-15} to a 0.1-m depth after 2 Myr.

Table 7-1 Time constant and microbial survival rate for representative depth and time of interest.

Depth (m)	TC (yr)	Microbial survival rate						
		1 (Kyr)	2 (Kyr)	3 (Kyr)	10 (Kyr)	0.1 (Myr)	1 (Myr)	2 (Myr)
1×10^{-4}	7.5×10^{1}	1.6×10^{-6}	2.6×10^{-8}	4.2×10^{-18}	1.2×10^{-58}	0	0	0
1×10^{-3}	3.0×10^{2}	3.4×10^{-2}	1.2×10^{-3}	4.0×10^{-5}	2.2×10^{-15}	0	0	0
1×10^{-2}	1.6×10^{4}	9.4×10^{-1}	8.8×10^{-1}	8.3×10^{-1}	5.4×10^{-1}	2.1×10^{-3}	1.5×10^{-27}	2.2×10^{-54}
3×10^{-2}	5.1×10^{4}	9.8×10^{-1}	9.6×10^{-1}	9.4×10^{-1}	8.2×10^{-1}	1.4×10^{-1}	2.8×10^{-9}	8.1×10^{-18}
5×10^{-2}	5.8×10^{4}	9.8×10^{-1}	9.7×10^{-1}	9.5×10^{-1}	8.4×10^{-1}	1.8×10^{-1}	3.2×10^{-8}	9.9×10^{-16}
1×10^{-1}	6.3×10^{4}	9.8×10^{-1}	9.7×10^{-1}	9.5×10^{-1}	8.5×10^{-1}	2.0×10^{-1}	1.2×10^{-7}	1.5×10^{-14}
3×10^{-1}	6.9×10^{4}	9.9×10^{-1}	9.7×10^{-1}	9.6×10^{-1}	8.6×10^{-1}	2.3×10^{-1}	4.6×10^{-7}	2.2×10^{-13}
5×10^{-1}	7.9×10^{4}	9.9×10^{-1}	9.7×10^{-1}	9.6×10^{-1}	8.8×10^{-1}	2.8×10^{-1}	3.1×10^{-6}	9.6×10^{-12}
1×10^{0}	1.4×10^{5}	9.9×10^{-1}	9.9×10^{-1}	9.8×10^{-1}	9.3×10^{-1}	4.8×10^{-1}	6.1×10^{-4}	3.8×10^{-7}

Table 7-2 Averaged microbial survival rate for representative sampling depth.

Depth (m)	Averaged microbial survival rate						
	1 (Kyr)	2 (Kyr)	3 (Kyr)	10 (Kyr)	0.1 (Myr)	1 (Myr)	2 (Myr)
1×10^{-4}	1.6×10^{-6}	2.6×10^{-12}	4.2×10^{-8}	1.2×10^{-58}	0	0	0
1×10^{-3}	5.1×10^{-3}	1.2×10^{-4}	3.6×10^{-6}	2.0×10^{-16}	0	0	0
1×10^{-2}	6.4×10^{-1}	5.1×10^{-1}	4.2×10^{-1}	1.7×10^{-1}	1.8×10^{-4}	1.1×10^{-28}	1.6×10^{-55}
3×10^{-2}	8.6×10^{-1}	8.0×10^{-1}	7.5×10^{-1}	5.6×10^{-1}	5.6×10^{-2}	3.7×10^{-10}	8.4×10^{-19}
5×10^{-2}	9.1×10^{-1}	8.7×10^{-1}	8.3×10^{-1}	6.7×10^{-1}	9.8×10^{-2}	6.2×10^{-9}	1.3×10^{-16}
1×10^{-1}	9.5×10^{-1}	9.2×10^{-1}	8.9×10^{-1}	7.6×10^{-1}	1.5×10^{-1}	4.5×10^{-8}	3.9×10^{-15}
3×10^{-1}	9.7×10^{-1}	9.5×10^{-1}	9.3×10^{-1}	8.3×10^{-1}	2.0×10^{-1}	2.1×10^{-7}	6.4×10^{-14}
5×10^{-1}	9.8×10^{-1}	9.6×10^{-1}	9.4×10^{-1}	8.4×10^{-1}	2.2×10^{-1}	6.6×10^{-7}	1.1×10^{-12}
1×10^{0}	9.8×10^{-1}	9.7×10^{-1}	9.6×10^{-1}	8.7×10^{-1}	3.7×10^{-1}	6.7×10^{-5}	2.4×10^{-8}

8. Mars Ejecta Formation and Transportation

8.1. Smoothed Particle Hydrodynamic (SPH) Analysis

Mass and velocity distribution of Martian materials ejected by impacts are the key to more precisely estimate the mass accreting on Martian moons. Here, we used a 3-dimensional Smoothed Particle Hydrodynamic (SPH) method (Lucy, 1977; Monaghan, 1992) to perform impact simulations. The SPH method can easily trace large deformations and shock waves, which are involved in planetary impact phenomena. Our numerical code is the same as that used in Kurosawa et al. (Kurosawa et al., 2018) and it can calculate a purely hydrodynamic flow without gravity and material strength.

We numerically calculated an impact of a spherical projectile with a radius of R_p = 10 km onto a flat target. For the numerical resolution, 5.2×10^5 SPH particles are used for the projectile, which corresponds to about 50 SPH particles per projectile radius. The equal-mass SPH particles are used for the target. The Tillotson EOS (Tillotson, 1962) with the parameter sets for granite (Allen, 1967) was used for both the projectile and target. For the impact conditions, we considered various impact velocities from 6 km/s to 18 km/s with the 3 km/s interval, and various impact angles from 15 degrees to 90 degrees (vertical impact) with the 15 degrees interval. In total, 30 impact simulations were performed. Although just one set for the impactor radius was considered, we are able to convert our results to any size of impactor, because all hydrodynamic equations can be rewritten in a dimensionless form in cases without gravity and strength (e.g., Johnson and Melosh, 2013).

Figure 8-1 shows the temporal evolutions for particle velocity (i.e., ejection velocity) and pressure for the 45-degrees impact with the impact velocity at 12 km/s. Figure 8-2 shows the ejected mass of the target materials (i.e., Martian materials) whose ejection velocity exceeds 3.5 km/s. Note that the velocity of more than 3.8 km/s is need for ejected materials to reach the orbit of Phobos. In this work, the radius of Phobos is expressed to be 50 times larger in order to save the computational cost for estimating the collision probability of these ejected materials on Phobos. Therefore, here we used 3.5 km/s for the threshold instead of 3.8 km/s.

Figure 8-2 shows that the ejected mass normalized by the impactor mass (M_{imp}) increases with the impact velocity, and has a peak at the impact angle of 45 degrees. At the same impact velocity, the ejected mass for 45 degrees is more than that for 90 degrees vertical impact by a factor of more than 3. It is also noted that when producing the same sized crater with the same impact velocity (see Eq. 8-1 エラー! 参照元が見つかりません。エラー! 参照元が見つかりません。エラー! 参照元が見つかりません。エラー! 参照元が見つかりません。エラー! 参照元が見つかりません。 in Section 8.2), the impactor size should increase by ~1.15 times (or impactor mass should increase by 1.15 to 1.5 times) at 45-degrees impact compared to 90-degrees impact. Therefore, the ejection mass is increased by ~3×1.5=4.5 times to produce the same crater with the same impact velocity at 45-degrees impact compared to 90-degrees impact.

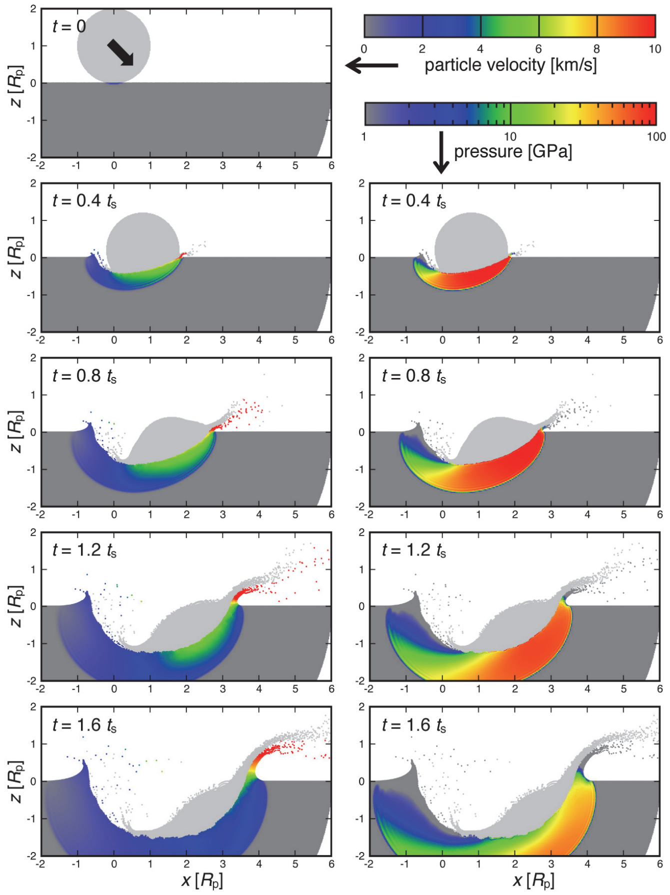

Fig. 8-1. Snapshots for 45-degrees impact at 12 km/s.

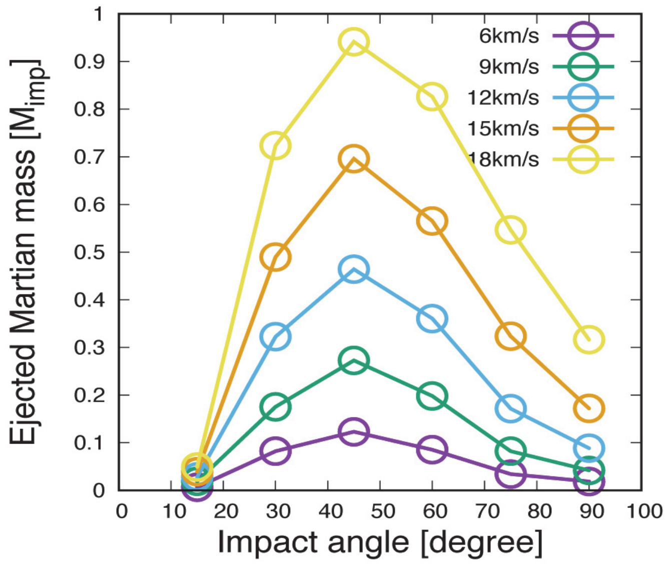

Fig. 8-2 Ejected Martian mass normalized by the impactor mass for various impact angle (x-axis) and velocity (by color).

8.2. Crater-Forming Impact Conditions

We considered five fresh craters found on Mars as the sources of Martian rocks on the moons. The locations and diameters are summarized in Table 8-1. We searched the set of the impact conditions, which are characterized by projectile diameter D_p, impact velocity V_{imp}, and impact angle θ_{imp} measured from the horizontal, using a Monte Carlo approach to investigate the effects of the stochastic nature of the impact events. The size distribution of the impactor was taken from the crater size-frequency distribution (e.g., Hartmann, 2005). We assumed that the impact velocity distribution can be approximated as a Rayleigh distribution (e.g., Zahnle et al., 2003; Parkos et al., 2018). The mean impact velocity onto Mars was estimated to be 14 km/s by assuming the dynamical transports of the impactors from ν_6 mean motion resonance in the Main-belt region (Ito and Malhotra, 2006). The impact angle distribution was taken from $\sin(2\theta_{imp})$ (Shoemaker, 1962). To combine with the impact conditions employed in the SPH simulation in Section 8.1, we obtained the impact velocities and angles discretely from the original distributions. The ranges of impact velocity and angle were set to from 6 km/s to 18 km/s at a step of 3 km/s and from 15 degrees to 90 degrees stepping by 15 degrees, respectively.

The transient crater diameter D_{tr} under a gravity-dominated regime was calculated by the π-group scaling laws (e.g., Schmidt and Housen, 1987) as follows.

$$D_{tr} = \left(\frac{\pi}{6}\right)^{\frac{1}{3}} C_D \left(\frac{4\pi}{3}\right)^{\frac{\beta}{3}} \left(\frac{\rho_p}{\rho_t}\right)^{\frac{1}{3}} D_p^{1-\beta}\, g^{\beta} \left(V_{imp} \sin \vartheta_{imp}\right)^{2\beta} \tag{8-1}$$

where $C_D = 1.4$, $\beta = 0.17$, $\rho_p = 2.7 \times 10^3$ kg/m³, and $g = 3.7$ m/s² for Mars are a dimensionless scaling constant, a dimensionless scaling exponent, projectile density, target density, and gravitational acceleration, respectively. The scaling parameters correspond to the values for dry sand (Schmidt and Housen, 1987). We assumed that a projectile and the Martian crust are basaltic rocks. An empirical equation was employed to estimate the final crater diameter D_f from the transient diameter as follows.

$$D_f = 1.2\, D_c^{-0.13}\, D_{tr}^{1.13} \tag{8-2}$$

Table 8-1 The locations and the diameters of five fresh craters on Mars considered in this study.

Name	Latitude (deg)	East Longitude (deg)	Diameter (km)	Estimated age (Myr)
Mojave	7.57	327.4	58	3–5[a]
Tooting	23.4	207.5	29	2–10[b]
McMurdo	-84.5	0.0	23	2–30[b]
Corinto	16.9	141.7	13.5	2[c]–3.2[d]
Zunil	7.7	166	10.1	0.1–1[b]

Notes: [a] Werner et al. (2014) based on a crater chronology model.
[b] Hartmann et al. (2010) based on a crater chronology model.
[c] Hartmann et al. (2010) based on the data by Malin et al. (2006)
[d] Golombek et al. (2014) based on the superposition relationship between the Corinto secondaries and the older-dated lava unit.

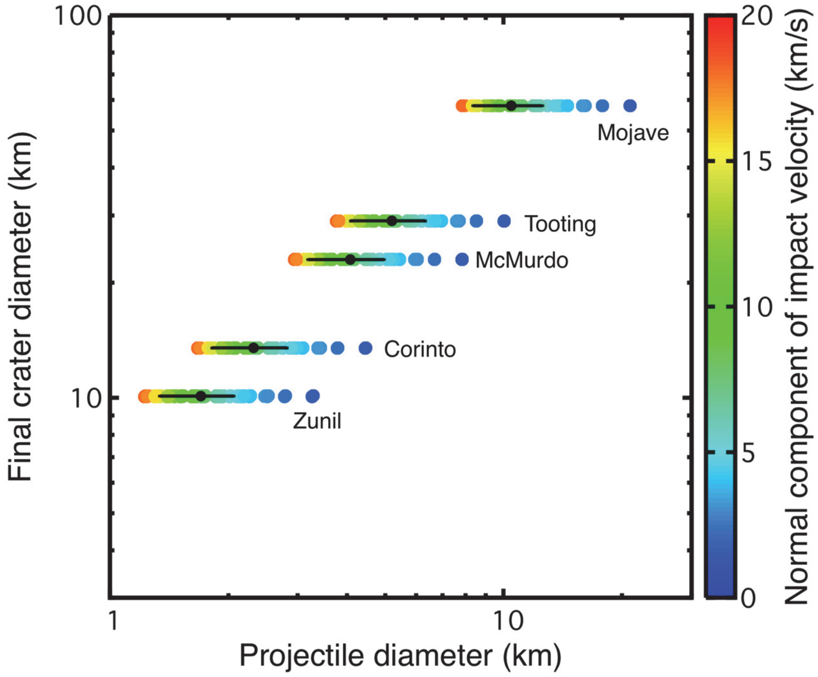

Fig. 8-3 The calculated final crater diameter as a function of projectile diameter. The color scale shows the normal component of impact velocity. Each crater name is also shown in the figure. The averaged projectile diameters and their standard deviations are shown in the figure as the black filled circles with error bars.

where D_c is the transition diameter from simple craters to complex ones (e.g., McKinnon et al., 1991). The transition diameter D_c on Mars was estimated to be 7 km based on the data compilation of the depth-to-diameter ratios of observed craters on terrestrial planets (Pike, 1988). We extracted 10,000 events for each crater on Mars, which reproduce the observed diameters within ±0.03 km, from the Monte Carlo calculations (Fig. 8-3). Hereafter, we used the averaged values of the projectile diameters. The standard deviations in the projectile diameters are ~20%. The calculations described above provides the absolute values of the total mass of the high-speed ejecta, which reaches Martian moons, by a combination with the scale-adjustable hydrocode calculation as discussed in Section 8.1.

8.3. Trajectory Analysis

In this work, we randomly choose combinations of crater-forming impact parameters (V_{imp}, M_{imp}, θ_{imp}) and orbital phase of Martian moon (the orbital plane is assumed to be on equatorial plane of Mars). In the case of 5 large craters discussed above, we fixed the locations of impacts at the current locations. The impact direction on Mars is randomly chosen except for Zunil. Since Zunil crater is the known-youngest ray craters with a diameter larger than 10 km in diameter (Tornabene et al., 2006), the geology of Zunil and the area around the crater, including the spatial distribution of the ray system and the secondary craters, has been extensively studied (e.g., Tornabene et al., 2006; McEwen et al., 2005; Preblich et al., 2007; Hartmann et al., 2010). It has been constrained that Zunil crater was formed by a moderately oblique impact from the east-northeast (Preblich et al., 2007). Thus, the impact direction for Zunil crater in our model was chosen from the northeast to the east. In the case of the fully randomized case, latitude and longitude of the impact location on Mars are randomly distributed all over the surface of Mars. At each 5 large craters and the fully randomized case where impact locations are randomly distributed through the surface of Mars, we perform 10,000 times of Monte Carlo simulations, respectively.

Using the selected crater-forming impact parameters, we derive positions and velocities of the ejecta from the data obtained by SPH impact simulations in section 8.1. Then, we pass this information to the orbital calculation as inputs. In the orbital calculation, we assume that the ejecta and Martian moons are massless point particles since they are significantly small compared to Mars. Phobos and Deimos are assumed to have circular orbits with the current semi-major axes. Single orbits of ejecta and Martian moons are analytically solved by considering two body problem with Mars – in the two-body problem, we can solve location and velocity at arbitrary time if we know initial position and velocity of the particle (e.g. Murray and Dermott, 1999). In order to increase the resolution of the impact detection, we inflate moons' diameter by 50 times (inflation factor of $f = 50$) but we confirm that the results do not significantly changed when $f<100$ (the final results presented below are scaled by f^2).

We detect collision when relative distance between Martian moon and ejecta is smaller than the radius of the moon. We confirm that the outcome obtained from our two-body analytical approach is consistent with that obtained from direct N-body calculation where orbits of test-particles are integrated numerically under the gravity of Mars (the same N-body code is used in Hyodo et al., 2015; Hyodo and Charnoz, 2017). Since N-body calculation is time consuming, we use the above analytical approach in this work.

8.4. Orbital Evolution of Ejecta

In this section, we present the results of our Monte Carlo simulations. Below we discuss the distribution of impact velocity of ejecta to Martian moons and the amount of mass that are transferred from Mars to Martian moons.

8.4.1. Impact Velocity to Phobos

Figure 8-4 shows the cumulative fraction of impact velocity of the ejecta to Phobos. Most of the ejecta has impact velocity between ~1-20 km/s and only small fraction of the ejecta has impact velocity smaller than ~2 km/s. The outcome strongly depends on the latitude of the crater-forming event – for example, Mojave and Tooting share similar distribution but McMurdo shows largely different distribution from the others. Since McMurdo is located close to the south pole of Mars, the orbits of ejecta launched from McMurdo and reach Phobos always cross the orbits of Phobos from the direction perpendicular to the orbital plane. Thus, the impact velocity becomes higher than the orbital velocity of Phobos (~2 km/s). Also, when ejecta has hyperbolic orbits from McMurdo ($v_{\mathrm{eje}} >$ ~5 km/s and corresponding orbital velocity at the location of Phobos is $v_{\mathrm{imp}} >$ ~3 km/s), they cannot reach Phobos because such high-speed ejecta can reach the orbital plane of Martian moons (equatorial plane of Mars) only at much farther distance to Mars from this high latitude. Therefore, the impact

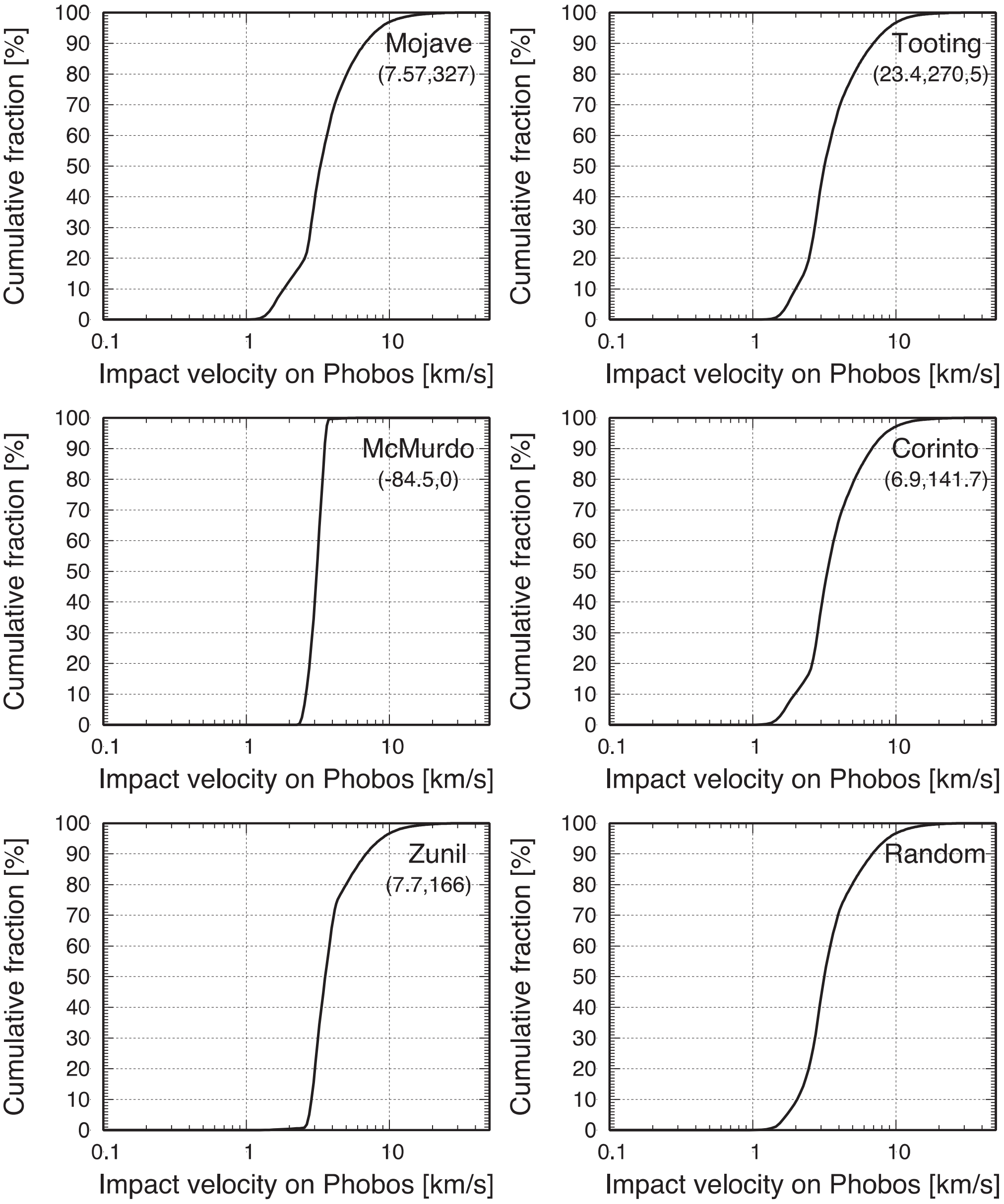

Fig. 8-4 Cumulative distribution of impact velocity to Phobos as a function of impact velocity to Phobos. From left to right and from top to bottom panels, the cases of Mojave, Tooting, McMurdo, Corinto, Zunil and the fully random case are shown respectively. Solid line represents impact velocity. The latitude and longitude of each crater is also shown beside the crater name.

velocity is limited in a narrow range between around ~2-3 km/s in the case of McMurdo-forming impact (see Fig. 8-4 left middle panel). In the case of the fully randomized case, the impact velocity to Phobos is between ~1-20 km/s as seen in other cases. The sudden change of the distribution around v_{imp}~3 km/s is due to the change of orbits from eccentric ($v_{eje} <$ ~5 km/s) to hyperbolic ($v_{eje} >$ ~5 km/s). As for Zunil-forming impactor, since we have limited impact direction to those from east-northeast, the ejecta is produced to the west-northwest direction. On the other hand, the orbital directions of Phobos and Deimos are from west to east. Therefore, the ejecta

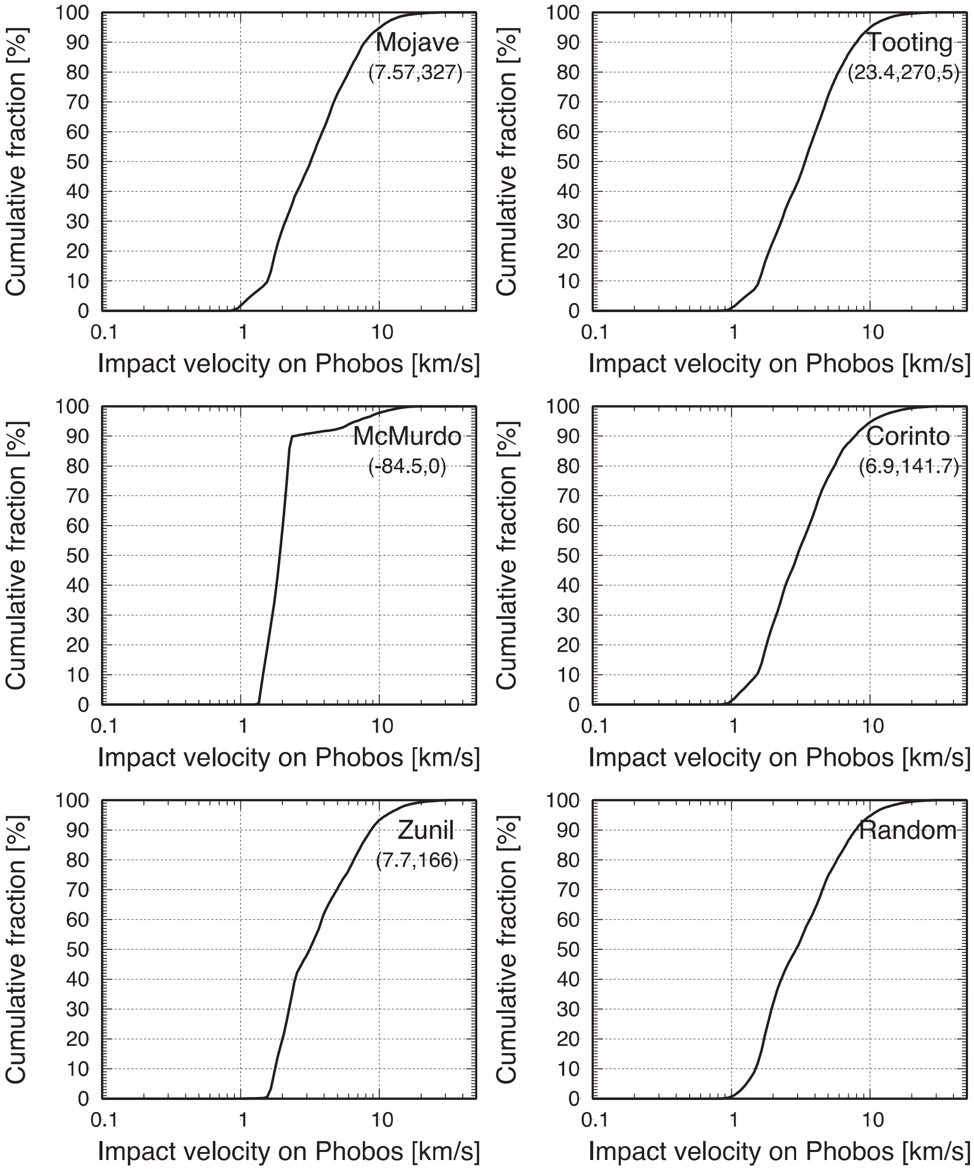

Fig. 8-5 Same as Fig. 8-4 but for Deimos.

experiences nearly head-on collisions with Phobos. Thus, the impact velocity becomes larger than orbital velocity of Phobos (~2 km/s, see Fig. 8-4 left bottom panel).

8.4.2. Impact Velocity to Deimos

Figure 8-5 shows cumulative distribution of impact velocity of the ejecta to Deimos. The overall trends are similar to what we see in the case of Phobos (Fig. 8-4) but the minimum impact velocity is shifted to the smaller values. This is because the orbital radius of Deimos from Mars is larger than that of Phobos and thus the relative velocity becomes smaller since both orbital velocity of Deimos and ejecta become smaller as they become

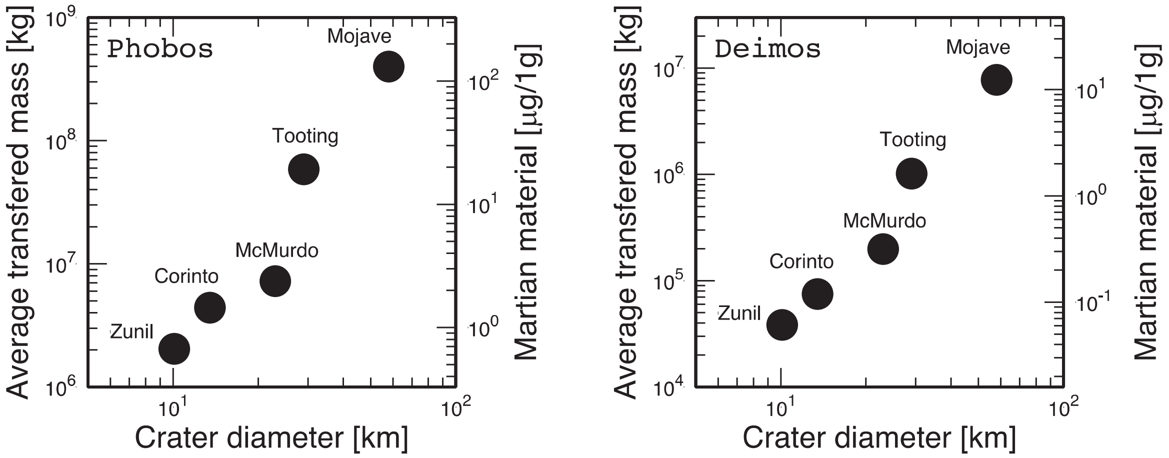

Fig. 8-6 The average transferred mass from Mars to Martian moons (left panel: Phobos, right panel: Deimos) after our 10,000 times of Monte Carlo simulations. Right-side vertical axis represents the mixing ratio of the Mars ejecta to the surface materials of Martian moons by assuming the mixing depth of 1 m and homogeneous mixing.

further from Mars. The change of the slope of the distribution at around v_{imp} ~1.8 km/s is due to the change in orbits of ejecta from eccentric to hyperbolic.

8.4.3. Mass Transfer from Mars to Martian Moons

Here we discuss the amount of ejecta that is transferred from Mars to Martian moons. Figure 8-6 shows the averaged-total transported rocks from the five recent craters on Mars and the sum of the average-total masses are found to be ~4.7 x 10^8 kg for Phobos and ~9.1 x 10^6 kg for Deimos, respectively. If the uniform mixing of the Martian rocks with the Phobos regolith down to 1 m depth is assumed (Chappaz et al., 2013; Ramsley and Head, 2013), the mixing ratio of the Martian materials to the Phobos regolith is estimated to be ~150 ppm. By following the same procedure, we estimate the mixing ratio of the Martian materials to the Deimos regolith to be ~9 ppm. This mixing ratio of Phobos is ~2 orders of magnitude than the previous estimate (~2 ppm, Chappaz et al., 2013). This upward revision is mainly come from the consideration of the Mojave-forming event where the previous study neglected and considered only other 4 large craters. This is because at the time the previous paper is published, the formation age of Mojave had not been constrained well, and the age was recently determined as 3-5 Myr (Werner et al. 2014). In addition, since we have used realistic impact conditions and 3-D SPH simulations to obtain initial position-velocity distributions of the ejecta, the total ejection mass is increased by a factor of about ~4.5 at 45-degrees impact compared to 90-degrees impact and mass distribution is increased by several factors at high impact probability regime around v_{eje}~4.2 km/s (see Fig. 8-7). Due to these two effects, the net transferred mass to Phobos is increase by 1-order at a single crater-forming event compared to the previous works (Chappaz et al., 2013; Ramsley and Head, 2013) where impact is limited to the head-on impact (impact angle of 90 degrees) and where the ejecta mass and velocity distribution are based on analytical method, and ejection direction is assumed to have simple cone-shape distribution.

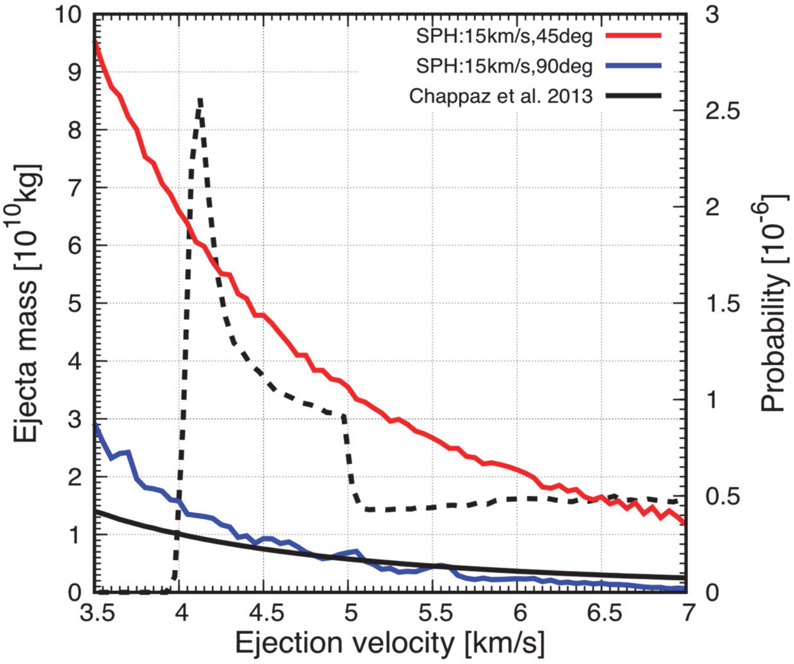

Fig. 8-7 Ejecta mass distribution as a function of ejection velocity (bin size is 0.05 km/s) to form Zunil-sized crater. Black line represents that obtained by the same procedure employed in Chappaz et al. (2013). Blue and red lines represent those of our SPH simulations (45-degrees and 90-degrees impact), respectively. Right-side vertical axis represents impact probability as a function of ejection velocity and black dashed line represents typical impact probability in the case of the fully randomized case. Around the peak of impact probability (V_{eje} ~ 4.2 km/s), SPH simulations show mass distribution larger than that of Chappaz et al.

9. Distribution of Mars Ejecta Fragments over Martian Moons

We discuss impact bombardment of the microbial Mars rocks on each of the moons and the fate of the transported microbes in this section. We focused only on the Zunil crater in the following analyses as the following reasons. In Section 7, we clearly showed that the microbes must be sterilized within 2 Myr down to 0.1 m from the surface. Thus, we neglected the contribution by the larger craters, such as Corinto (13.8 km), McMurdo (23 km), Tooting (29 km), Mojave (58 km) and so on, to the microbe transport. The formation ages of the above craters have been estimated older than 2 Myr (Malin et al. 2006; Hartmann et al., 2010; Golombek et al., 2014; Werner et al., 2014). The Zunil is the youngest-known ray craters with a diameter larger than 10 km on Mars. Ray systems around the host crater is thought to be one of the most prominent signatures of fresh craters on planetary bodies (e.g., Hawke et al., 2004). A lower limit of the formation age of Zunil has been estimated to be 0.1 Myr based on the crater chronology (e.g., Hartmann et al. 2010). Although there are ~10 smaller-young-ray craters on Mars with similar formation ages (Tornabene et al. 2006; Hartmann et al. 2010), their contributions to the microbe transport is likely to be neglected compared to the Zunil event because the transported mass from Mars to the moons is roughly proportional to the cubic of the crater diameter.

We assumed that all the microbial Mars rocks are spheres 10 cm in diameter in this study because the size-frequency distribution (SFD) of the ejected Mars rocks is highly uncertain. This size corresponds to a minimum size required for penetrating the Martian atmosphere into the space (e.g., Artemieva and Ivanov, 2004, and also Section 5). This assumption yields an upper limit of the cumulative surface area of the resultant impact craters on the regolith covering on each of the moons because it is controlled by frequent impacts by small impactors. In contrast, the mixing depth of the microbes in moons' regolith would be a minimum under this assumption. Consequently, for Zunil case, the total mass of the Martian ejecta colliding Phobos and Deimos is 2.0×10^6 kg and 3.8×10^4 kg (see Fig. 8-6), respectively, which leads that the total numbers of impacts N_{total} to Phobos and Deimos were estimated as 1.4×10^6 and 2.7×10^4, respectively, with the projectile density $\rho_{\mathrm{p}} = 2.7 \times 10^3$ kg/m^3.

We used a Monte Carlo approach to include the distributions of impact velocity and angle calculated by the numerical simulations described in Section 8. We randomly assigned impact velocity and angle to each microbial rock from the distributions. This treatment allows us to characterize each impact event. The impact outcomes under a given set of impact conditions can be estimated by using a number of previous studies in the field of impact physics. Figure 9.1. shows the cumulative frequency distributions of the impact angle (Fig. 9.1) actually used in this calculation. The results for both Phobos and Deimos are shown in the figure. The impact velocity distributions were taken from the data shown in Figs. 8.4. and 8.5.

9.1. Crater Formation

Hypervelocity impacts of Mars rocks onto each surface of the moons should produce impact craters (e.g., Melosh, 1989). In this study, we assumed that all impacts of Mars rocks on each of the moons occur on a regolith layer because each surface of the moons is globally covered by a regolith layer with a thickness of >20 m (e.g., Thomas, 1998). In addition, we also assumed that the cratering processes on the moons are controlled by the gravity rather than the strength of regolith layer. The assumption about the gravity-dominated regime would be reasonable because granular materials have low strength in general.

The longitudinal stress in a penetrating projectile into the regolith layer is likely to exceed the compressive strength of the microbial Mars rocks. For example, the compressive strength of intact basaltic rocks on Earth are reported as 0.17-0.48 GPa (e.g., Mizutani et al. 1990). In contrast, the dynamic ram pressure $P_{\mathrm{ram}} \sim \rho_{\mathrm{t}} v_{\mathrm{imp}}^2/2$ is estimated to be 1-10 GPa for impacts at 1-3 km/s, where $\rho_{\mathrm{t}} \sim 2 \times 10^3$ kg/m^3 is the density of the regolith (e.g., Andert et al. 2010). Thus, the Mars rocks are expected to be disrupted into fine fragments during a penetration. A part of fragments is likely to stick around the wall of the growing crater (e.g., Elbeshausen et al. 2013; and see also Fig. 8.5 in Section 8) and likely to mix with the regolith particles (e.g., Ebert et al. 2014; Daly and Schultz, 2016). After a transient crater formation, the wall of the transient crater collapses due to the gravity, resulting in a granular flow to the crater center. This is often referred to as the "modification stage" in the cratering processes (e.g., Melosh, 1989). During the collapse, the crater diameter/depth gradually increase/decrease to satisfy the mass conservation (e.g., Melosh, 1989). Note that such modification process should occur under the weak gravity field of each of the moons as well under the gravity-dominated cratering regime although the characteristic time for the modification becomes somewhat longer due to the small gravity. Hereafter, the produced volume lying the crater floor is referred to as the “collapsed lens”. The granular flow would enhance the mixing between the microbial-rock fragments transported from Mars and the regolith. Thus, we assumed that the retained Mars-rock fragments are homogeneously mixed into the collapsed lens deposited on the floor of the final crater. Hereafter, the resultant craters by impacts of the Mars rocks are referred to as “Mars-rock craters”. The counterpart of the retained volume of the projectile would fly away from the crater. The fate of this fraction is discussed in Section 9.2.

To investigate the microbe concentration of the collapsed lens in a Mars-rock crater, the fraction of the projectile retention ψ is necessary. Unfortunately, the dynamics of projectile deformation and fragmentation during impact processes has not been fully understood. In this study, we employed the experimental data by Daly and Schultz (2016). Although the impact velocity was fixed at 4.5–5 km/s in their experiments, which is higher than the averaged impact velocity of the Mars rocks, they provided a systematic data set of ψ against the change in the impact angle from 30 to 90 degrees measured from the target surface. We derived an empirical formula by a combination between the data set and the two physical constraints, which are (1) $\psi = 0$ at the impact angle θ_{imp} = zero and (2) $\mathrm{d}\psi/\mathrm{d}\theta_{\mathrm{imp}} > 0$, as follows.

$$\psi = 0.718 - 1.01\cos\vartheta_{\mathrm{imp}} + 0.294\cos^2\vartheta_{\mathrm{imp}}. \tag{9-1}$$

According to the orbital calculations described in Section 8.4, the impact angle of Mars rocks onto Phobos and Deimos is likely to be nearly isotropic (see Fig. 9-1). By convoluting with the θ_{imp} frequency distribution, the averaged retained fraction ψ_{ave} of the Mars rocks in the final crater on Mars was estimated to be 22% for Phobos and 29% for Deimos.

The total mass of the collapsed lens M_{c} in a Mars-rock crater was roughly estimated by considering the geometries of the transient and final craters (Melosh, 1989, pp.129). There are three assumptions used to calculate M_{c}: (1) The shape of both transient and final crater is a parabola-shape, (2) the depth-to-diameter ratio of the final crater is 0.2, (3) the depth of the transient crater H_{tr} is the sum of the depth of the final crater H_{f} and the thickness of the collapsed lens H_{c}. Figure 9-2 shows a schematic cross section of the final crater considered here. Using these assumptions, we can estimate M_{c} as follows,

$$M_{\mathrm{c}} = \frac{\pi}{80}\rho_{\mathrm{t}} D_{\mathrm{f}}^3, \tag{9-2}$$

where D_{f} is the diameter of the final crater. We can estimate D_{f} under a given set of impact conditions by using the π-group scaling law and an empirical relation connecting the transient crater diameter D_{tr} with D_{f} (e.g., Melosh and Vickery, 1989) as follows,

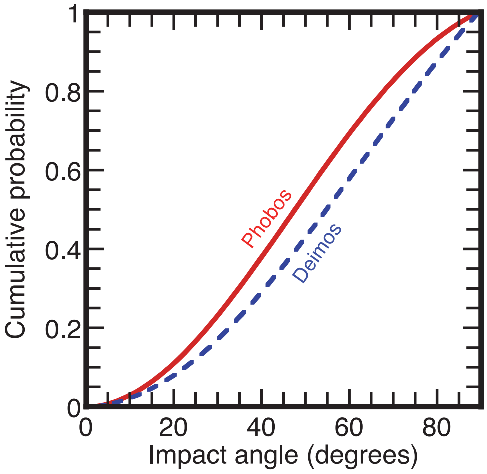

Fig. 9-1 The cumulative frequency distribution of impact angles of Mars rocks onto Phobos (Red solid line) and Deimos (blue dashed line)

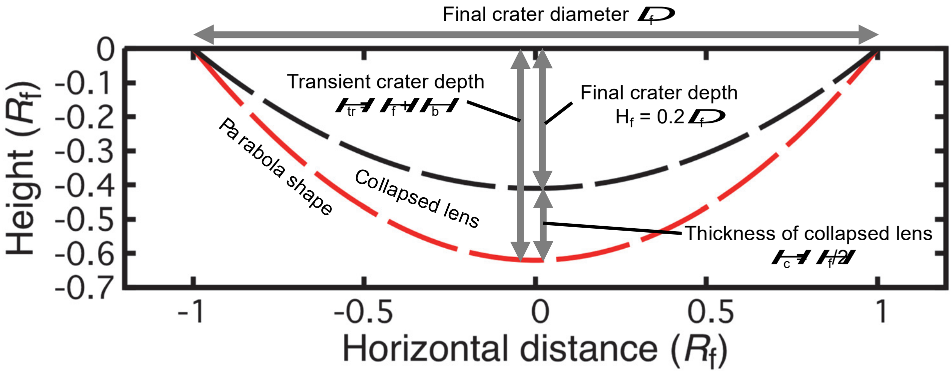

Fig. 9-2 A schematic cross section of Mars-rock craters considered in this study. The black dashed line is the profile of the final crater actually formed on the regolith. The red shaded region corresponds to the collapsed lens where the Mars-rock fragments mix with the moon's regolith particles.

$$D_f = 1.25 D_{tr}, \tag{9-3}$$

and the transient crater diameter is given by Eq. (8-1), but g = 0.0057 m/s^2 for Phobos and g = 0.003 m/s^2 for Deimos were used here. A typical value of D_f in the Monte Carlo calculation was ~10 m, which is two orders of magnitude than D_p. The small gravitational acceleration on the surfaces of Phobos and Deimos largely contribute to this size enhancement. The thickness of collapsed lens H_c can be also estimated using D_f as $H_c \sim 0.1 D_f \sim 1$ m. The H_c value imply that the typical mixing depth of the Mars rocks is ~1 m, which is an order of magnitude than D_p. The same parameters used in Eq. (8-1) were employed here except that the target density ρ_t was set to $\rho_t = 2 \times 10^3$ kg/m^3. The mixing ratio of the Mars rocks to the regolith was ranged from ~10 ppb to ~100 ppm in our Monte Carlo calculations.

Since the surface area of a collapsed lens is equivalent to that of the host crater, the ratios of the cumulative surface area of the final crater $S_{\mathrm{total}} = \sum \pi D_{\mathrm{f}}^2$ to the surface areas of the moon S_{moon} correspond to the access probability to the Mars-rock craters P_{crater} when we consider a random sampling of the moon'sregolith from somewhere on the surfaces. In our model, P_{crater} on Phobos and Deimos were 3.4% and 0.28%, respectively. Note that the data scatter of P_{crater} in different runs is relatively small (< 0.1%). Although each size of the final crater was ranged from 3 m to 12 m due to the differences in v_{imp} and θ_{imp} at each impact, such dispersion is canceled out the summation of all the impacts.

9.2. Scattered Fragments

In the previous section, we modeled that a part (20-30 %) of a microbial Mars rock mixes into a collapsed lens lying on the Mars-rock crater. Here, we discuss the fate of the materials ejected from Mars rock craters, which has 70–80% of mass in the entire transported Mars rocks. In the case of oblique impacts, projectiles have a large horizontal component of the impact velocity parallel to the target surface compared to the escape velocities v_{esc} of the moons (11 m/s for Phobos and 6.9 m/s for Deimos). In contrast, the escape velocities from the Mars system at the orbits of the moons are the same orders of magnitude (3 km/s for Phobos and 4 km/s for Deimos) of the impact velocity of the Mars rocks as shown in Figs. 8.4 and 8.5. Therefore, the destructed projectiles are expected to escape from the local gravity field from each of the moons and disperse into orbits around Mars. The ejected-moons-regolith particles from the Mars-rock craters are also injected into the dust torus produced at a similar semi-major axis of each of the moons. The mass of dispersed projectile $M_{\mathrm{dis,p}}$ and the escaped mass of the regolith particles $M_{\mathrm{dis,t}}$ (e.g., Housen et al. 1983) are given by

$$M_{\mathrm{dis,p}} = (1-\psi)M_{\mathrm{p}}, \tag{9-3}$$

and

$$M_{\mathrm{dis,t}} = C_{\mathrm{V}}\rho_{\mathrm{t}}R_{\mathrm{tr}}^3\left(\frac{v_{\mathrm{esc}}}{\sqrt{gR_{\mathrm{tr}}}}\right)^{-3\mu}, \tag{9-4}$$

where $C_{\mathrm{v}} = 0.32$, $R_{\mathrm{tr}} = 0.5D_{\mathrm{tr}}$, and $\mu = 0.4$ are a scaling constant, transient crater radius, and the velocity-scaling exponent, respectively, and v_{esc} is the escape velocity from each of the moons (11 m/s for Phobos and 6.9 m/s for Deimos). The Eq. (9-4) is given by the Point-source theory (e.g., Holsapple and Schmidt, 1982; Housen et al. 1983). Typical values of $M_{\mathrm{dis,p}}$ and $M_{\mathrm{dis,t}}$ are ~1 kg and ~10^2 kg, respectively, resulting in the mixing ratio of the Mars-rock fragments to the regolith from Phobos or Deimos in a dust torus is likely to be ~1%.

The ejected particles re-accumulate onto Phobos and Deimos (e.g., Ramsley and Head, 2013) because the moons sweep out their own dust torus. It is difficult to estimate the time scale of the re-accumulation accurately without detailed numerical simulations considering ejection process and orbital evolution of ejected materials. Nevertheless, the time scale may be much longer than one orbital period of Phobos and Deimos (~ 10 hours and ~ 30 hours, respectively). On the other hand, most of the Mars rocks ejected from the Martian surface hit on

Phobos and Deimos within the orbital periods of Phobos and Deimos according to the orbital calculations in Section 8. The Mars rocks that did not hit on Phobos and Deimos accrete onto Mars within their just one orbital period, because they were launched from the Martian surface, so that they should return to Mars. Otherwise, they should escape from Mars gravity if they have very high ejection velocity (> 5 km/s). Thus, we assumed that the dispersed materials re-accumulate onto the uppermost surface of Phobos and Deimos after the cease of the Mars-rock bombardment.

The dispersion and re-accumulation of dust particles lead to form a global thin layer on each of the moons. The thickness of the thin layer on each of the moons was estimated to be 30 μm for Phobos and 1 μm for Deimos by using the total mass of the dust torus (~$100\Sigma M_p$) and the surface area of each of the moons. In above estimate, we assumed a homogeneous dispersion of infinitesimal particles onto the surfaces of Phobos and Deimos. This thickness estimate, however, is expected to be unlikely because such small particles (~1 μm) are removed from the Mars system prior to the re-accumulation due to radiation pressure within several hours (e.g., Ramsley and Head, 2013; Hyodo et al., 2018). Since actual sizes of the particles in the dust torus highly uncertain, we assumed that the thickness of the thin microbial layer is ~0.1 mm in this study. This assumption does not change the conclusion of this study unless the thickness is thicker than 0.3 mm because the time constant *TC* for radiation-induced sterilization is nearly constant (71 years) for the layer with a thickness of < 0.3 mm (Patel et al. 2017 and also see Section 7).

9.3. Surface Reformation by Meteoroid Impacts

In the previous section, we showed that the escaped Mars rocks from the host craters are expected to form a global thin layer with a thickness <0.1 mm. Table 7-2 clearly show the thin microbial layer on the uppermost surface suffer a rapid sterilization within ~2 x 10^3 years. Although the 70%–80% of the Mars rocks ejected from Zunil crater are likely to be mixed into this layer, this major fraction should be completely sterilized at the present. Nevertheless, the microbes in the thin layer could have survived up to the present if the microbes could be covered by a thick ejecta-deposit layer at a time in the past. Such “radiation shield” could be produced by “ordinary background impacts”, which are collisions of natural meteoroids with the moons. In this section, we discuss such the background impact flux onto each of the moons to assess the roles of the ejecta blanket forming radiation shield.

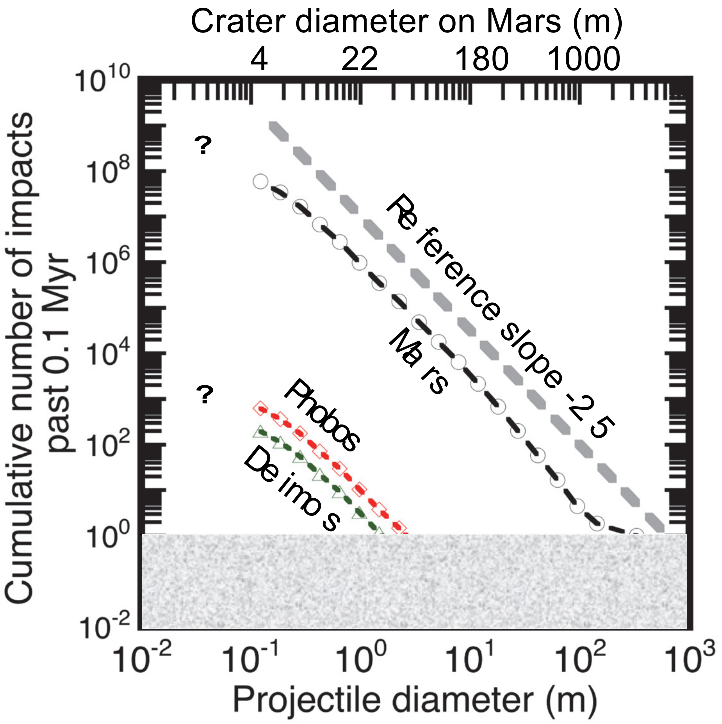

Fig. 9-3 The cumulative size-frequency impactor distributions (SFDs) pertaining to Mars, Phobos, and Deimos. The gray dashed line is also shown as a reference power-law function with the exponent of -2.5. The corresponding crater diameters on Mars are shown on the upper X-axis. Since the cumulative number of impactors *N* smaller than 0.1 m is unknown, the region is highlighted in grey and the question marks. The diameters at $N = 1$ corresponds to the maximum size of impactors during past 0.1 Myr. Although there is the possibility that impacts of the larger impactors occur on the moons, such events are statistically rare.

The impact flux of natural meteoroids onto Phobos and Deimos can be estimated based on the impact flux onto Mars. The crater SFD on the surface of Mars has been established well (e.g., Hartmann, 2005). The impactor SFD can be estimated from the crater SFD by using the relation connecting the impact/target conditions with the final crater diameter. The transient crater diameter D_{tr} on Mars can be also estimated by using the π-group scaling law (Eq. (8-1)). To convert from D_{tr} to D_f on Mars, we employed a combination between Eq (8-2) and Eq. (9-3). We employed the larger D_f calculated from two equations because we have to examine D_f against a wide range of D_p. The Eq. (9-3) could not be applied to too small craters although it is suitable for estimating the size of complex craters (McKinnon et al. 1991). The impactor SFDs for Phobos and Deimos were approximated by the products of the impactor SFD of Mars and the ratio of the geometric cross sections of the moons to that of Mars (e.g., Ramsley and Head, 2013). Figure 9-3 shows the impactor SFDs pertaining to Mars, Phobos, and Deimos at the surface age of 0.1 Myr. To convert from the crater SFD on Mars to the impactor one, averaged impact velocity and angle on Mars were used (14 km/s; Ito and Malhotra, 2006 and 45 degrees measured from the tangent plane; Shoemaker, 1962). The SFD can be approximated by a power-law form as

$$N\left(>D_\mathrm{p}\right)=D_\mathrm{pmax}^{2.5}D_\mathrm{p}^{-2.5}, \tag{9-5}$$

where $N(>D_\mathrm{p})$ and D_pmax are the cumulative number of impactors with a diameter larger than D_p and the maximum diameter of impactors, respectively. The maximum diameter D_pmax is defined as the diameter at $N(>D_\mathrm{p}) = 1$. The D_pmax for Phobos and Deimos in the past 0.1 Myr were estimated to be 2.6 m and 1.6 m, respectively. Although the total number of impacts of bodies smaller than 0.1 m is unknown, we decided to extrapolate Eq. (9-5) to smaller diameters. The extrapolation might be reasonable because the exponent of -2.5 is close to the steady-state SFD in a self-similar collision cascade (Tanaka et al., 1996).

The v_imp distribution of natural meteoroids can be approximated by a Rayleigh distribution (e.g., Zahnle et al., 2003; Parkos et al. 2018). The most likelihood impact velocities onto Phobos and Deimos were estimated to be 13.4 km/s and 13.2 km/s, respectively, based on the averaged impact velocity onto Mars (14 km/s), the escape velocity from Mars (5 km/s), and the escape velocities of the Mars system from the moon's orbits (Schmedemann et al., 2014; Hirata, 2017). We employed the well-known $\sin(2\theta_\mathrm{imp})$ function as the impact angle distribution (Shoemaker, 1962) for both Phobos and Deimos.

To investigate the significance of the ejecta deposit covering the thin microbial layer, the rate of decrease in the thickness of the ejecta deposit with increasing distance along the surface from the host crater is necessary. If the thin microbial layer is covered by the ejecta deposit with a thickness of >3 mm within 2×10^3 years after the Zunil-forming event, the microbes may survive during 0.1 Myr (i.e., until now) as shown in Table 7-2. Thus, we estimate the total coverage of the ejecta-deposit layer with the thickness of >3 mm produced by the impacts of natural meteoroids in the reminder of this section. We also employed the π-group scaling laws in the gravity-dominated regime in the estimation.

The mass of ejecta at a velocity bin (v_ej, $v_\mathrm{ej}+\mathrm{d}v_\mathrm{ej}$) is given by (e.g., Housen et al. 1983),

$$m_\mathrm{ej}\left(v_\mathrm{ej}\right)\mathrm{d}v_\mathrm{ej} = 3\mu C_\mathrm{V}\rho_\mathrm{t}R_\mathrm{tr}^3\left(gR_\mathrm{tr}\right)^{\frac{3\mu}{2}}v_\mathrm{ej}^{-3\mu-1}\mathrm{d}v_\mathrm{ej}, \tag{9-6}$$

where v_ej and $\mathrm{d}v_\mathrm{ej}$ are ejection velocity and a small increment of v_ej, respectively. The values of μ and C_v were the same values as used in Eq. (9-4). The ballistic range of the ejecta at the bin R_b including the curvature effect is given by [e.g., Melosh, 1989]

$$R_\mathrm{b} = 2R_\mathrm{moon}\tan^{-1}\left[\frac{\left(\frac{v_\mathrm{ej}^2}{gR_\mathrm{moon}}\right)\sin\vartheta_\mathrm{ej}\cos\vartheta_\mathrm{ej}}{1-\left(\frac{v_\mathrm{ej}^2}{gR_\mathrm{moon}}\right)\cos^2\vartheta_\mathrm{ej}}\right], \tag{9-7}$$

where R_moon and θ_ej are the radius of Phobos or Deimos and the launch angle of the ejecta, respectively. We used θ_ej of 45 degrees measured from the target surface in this calculation (e.g., Melosh, 1989). The surface area of the ejecta landing site for the velocity bin S_ej is given by

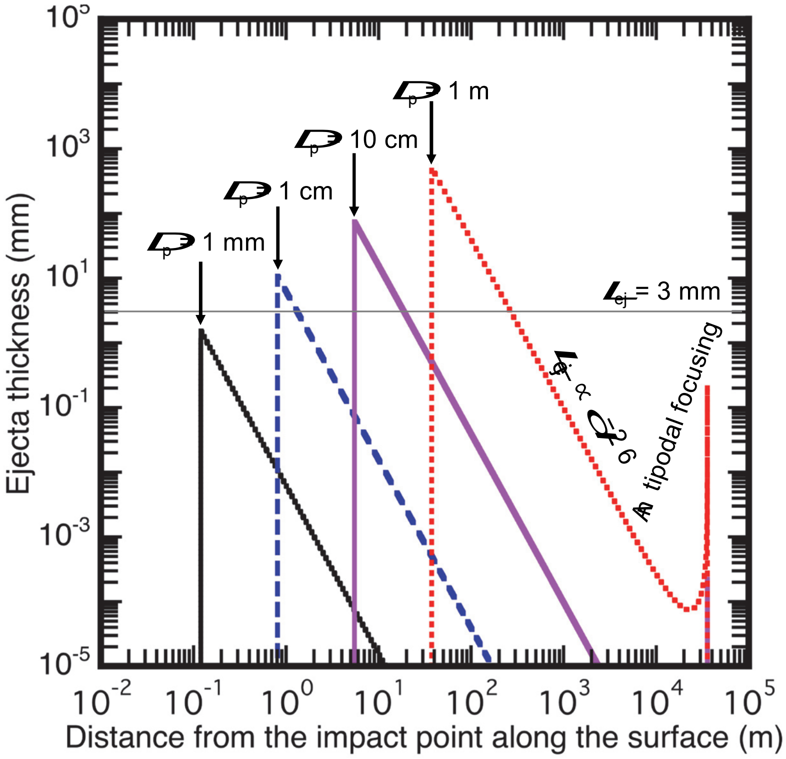

Fig. 9-4 The ejecta thickness as a function of the distance from the impact point along the surface of Phobos. We used D_p = 1 mm, 1 cm, 10 cm, and 1 m in this calculations. The grey horizontal line corresponds to the ejecta thickness of 3 mm.

$$S_{ej} = 2\pi R_{moon} \sin\lambda d\lambda, \tag{9-8}$$

where

$$\lambda = \frac{R_b}{R_{moon}}, \tag{9-9}$$

is the arc angle between the impact point and the ballistic range measured from the center of each of the moons. Consequently, the thickness of the ejecta deposit launched at the velocity bin L_{ej} can be obtained as

$$L_{ej} = \frac{m_{ej} dv_{ej}}{S_{ej} \rho_t}. \tag{9-10}$$

Figure 9-4 shows examples of the ejecta thickness on Phobos (g = 0.0057 m/s^2 and R_{moon} = 11 km) as a function of the distance from the impact point. We showed the results at four different D_p. The impact velocity and angle were set to the average values (13.4 km and 45 degrees). We set the ejecta thickness to be zero at the distance shorter than the final crater radius. The ejecta thickness decreases with increasing distance by following a power-law with an exponent -2.6. The exponent is consistent with the results of explosion experiments and numerical calculations (e.g., Melosh, 1989). We found that projectiles larger than $D_p > 1$ mm could produce a thick ejecta-deposit layer with the thickness of > 3 mm. Thus, the minimum diameter of natural meteoroids D_{pmin} was set to 1 mm. Although our model reproduces an antipodal focusing of the ejecta, the effects can be neglected because the thickness at the antipodal point is much less than 3 mm even when we considered a relatively large impactor with $D_p = 1$ m. Such the large impacts with $D_p > 1$ m statistically occur every 10^4 years on Phobos (Fig. 9-3). The total numbers of the impactors $N_{total,BG}$ within 2 x 10^3 years can be obtained by the impactor SFD and the values of D_{pmax} and D_{pmin} as

$$N_{total,BG} = \left(\frac{2 \times 10^3 \text{ years}}{0.1 \text{ Myr}}\right) D_{pmax}^{2.5} D_{pmin}^{2.5}. \qquad (9\text{-}11)$$

Since the impact rate on the Mars system in the past 3 Gyr is roughly constant (e.g., Neukum et al., 2001; Schmedemann et al. 2014), we simply multiply the cumulative number of impactors within 0.1 Myr by the ratio of t_{Req} for the uppermost surface to the time after the Zunil-forming event, where t_{Req} is the required time for complete sterilization by the radiation for the uppermost surface. The total numbers $N_{total,BG}$ for Phobos and Deimos were obtained as 6.7 x 10^6 and 2.0 x 10^6, respectively.

We used the same Monte Carlo model employed in the calculation of the Mars-rock bombardment (Sections 9.1 and 9.2) to estimate the total coverage of the thick-ejecta-deposit layer by combining the impactor SFD, $N_{total,BG}$ and the distributions of v_{imp} and θ_{imp}. The surface area of the thick ejecta-deposit layer S_{shield} is given by

$$S_{shield} = \pi\left(R_{b,3mm}^2 - R_f^2\right), \qquad (9\text{-}12)$$

where $R_{b,3mm}$ and R_f are the distance from the impact point covered by the thick ejecta-deposit layer along with the surface and the final crater radius, respectively. The ratio of the cumulative surface area of the thick ejecta layer S_{shield} to S_{moon} provides the access probability to the shielded microbial layer P_{layer}, where S_{moon} is the surface area of each of the moons (1.5 x 10^9 m^2 for Phobos and 5.0 x 10^8 m^2 for Deimos). We statistically obtained P_{layer} on Phobos and Deimos as 0.11 % and 0.097%, respectively, from the Monte Carlo runs. This means that 99.9 % of the microbes in the global thin layer should be sterilized within ~2 x 10^3 years after the Zunil-forming impact event.

10. Statistical Analysis of Microbial Contamination Probability

10.1. Major Crater Events

In the previous section, we described the fate of the Mars rocks after the transportation based on impact physics. The Mars rocks (~10 cm in diameter) are expected to be disrupted into fine fragments due to the impacts on the moon's surface. The 20-30% of Mars-rock fragments is entrained into the "collapsed lenses" lying on the floors of Mars-rock craters. The microbes in the retained Mars-rock fragments would be mixed well into

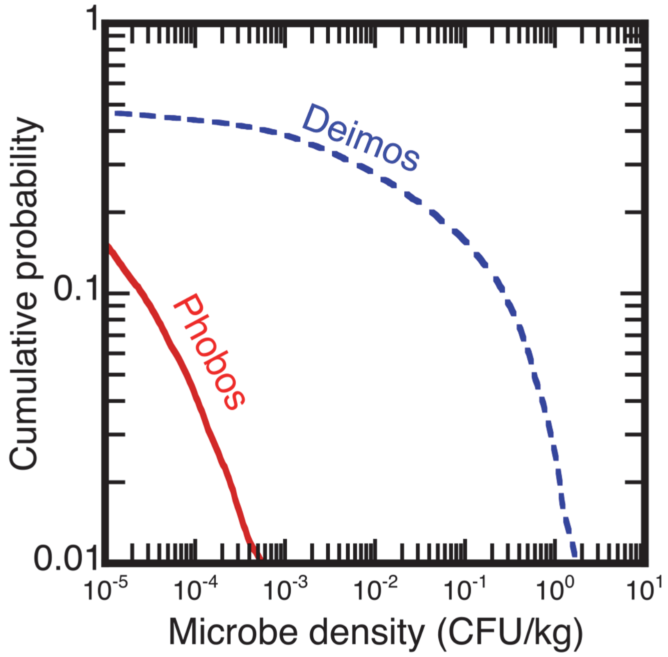

Fig. 10-1 The cumulative probability of the microbe concentration in the collapsed lens of Mars-rock craters. The results for Phobos (red solid line) and Deimos (blue dashed line).

the collapsed lenses. Since the thickness of the collapsed lens was estimated to be ~1 m, the microbes retained in the Mars-rock crater could have survived from the radiation up to the present. The counterpart of the Mars-rock fragments is once escaped from each of the moons and re-accumulated on the uppermost surface. The dispersion leads to form a global thin layer with a thickness of < 0.1 mm. Then, ~0.1% area of the global thin layer are protected from the radiation by the thick ejecta-deposit layer with a thickness of >3 mm. Hereafter, the covered portion is referred to as "the covered-microbial thin layer". In this section, we discuss the microbe concentration of the collapsed lens in the Mars-rock crater and the covered-microbial thin layer at the present day. Then, we assess the sampling probability of the microbes as functions of sampling depth, area, and mass.

First, we investigated the survival rate ξ (= N/N_0) of the microbes after each impact event by using the Eq. (6-2) with the nominal value for the parameters. The current model of impact sterilization cannot treat a θ_{imp} dependence on ξ. However, it should be note that the SterLim study (Summers, 2017) performed the impact experiments at two different impact angles 40 and 90 degrees measured from the target surface, and any systematic differences in ξ was not observed between the two angles. Thus, the averaged survival fraction ξ_{ave} was obtained simply by a convolution of the v_{imp} distribution with the survival rate ξ given by Eq. (6-2). We found that ξ_{ave} of the transported microbes for Zunil crater forming impact could be much lower than 0.1. In the cases of Phobos and Deimos, ξ_{ave} were 2.9×10^{-5} and 5.6×10^{-4}, respectively.

Second, we discuss about the Mars-rock craters. The microbe density of the collapsed lens in a Mars-rock crater n_{crater0} immediately after the crater formation is given by

$$n_{\mathrm{cratero}}=\frac{\xi n_{\mathrm{MR}}\psi M_{\mathrm{p}}}{(M_{\mathrm{c}}+M_{\mathrm{p}})}, \tag{10-1}$$

where M_{p} = 1.4 kg is the 10 cm-projectile mass and $n_{\mathrm{MR}} = 10^7$ CFU/kg is the microbe density in the Mars rocks immediately after the launch. Due to both impact sterilization and the dilution of microbial Mars rocks into a collapsed lens, n_{cratero} becomes well below n_{MR}. The averaged values of n_{cratero} after the bombardment on Phobos and Deimos were 3.1 x 10^{-3} CFU/kg and 4.8 x 10^{-2} CFU/kg, respectively. As discussed in Section 8.4, the averaged impact velocity onto Deimos (Fig. 8-5) is lower than that onto Phobos (Fig. 8-4), resulting in a higher averaged n_{cratero}. Figure 10-1 shows the cumulative frequency distributions of n_{cratero} for Phobos and Deimos. The distributions suggest that more than 90% for Phobos and 50% for Deimos of the collapsed lenses are sterilized down to 10^{-5} CFU/kg, which corresponds to the REQ-10 criterion for 100 g-sampling immediately after the crater formation. In contrast, there are Mars-rock craters with n_{cratero} higher than 1 CFU/kg on Deimos (~2%). Since the total number of the Mars rocks for Deimos is 2.7 x 10^4, the number of the craters with > 1 CFU/kg is estimated to be ~5 x 10^2.

Third, we discuss on the covered-microbial thin layer. The microbial column density immediately after the formation of the global thin layer σ_{thino} can be estimated as

$$\sigma_{\mathrm{thino}}=\frac{\xi_{\mathrm{ave}} n_{\mathrm{MR}}(1\text{-}\psi_{\mathrm{ave}})M_{\mathrm{p,total}}}{S_{\mathrm{moon}}}. \tag{10-2}$$

Our model yields σ_{thino} on Phobos and Deimos of 2.9 x 10^{-5} CFU/cm^2 and 3.3 x 10^{-5} CFU/cm^2, respectively. Then, the covering processes by the ejecta-deposit layer due to impacts of natural meteoroids is described as follows. During 2 x 10^3 years, which is the grace period against the radiation-induced extinction of the microbes in the global thin layer on the uppermost surface, the microbial column density $\sigma_{\mathrm{thin}}(t)$ rapidly decrease with time as

$$\sigma_{\mathrm{thin}}(t) = \sigma_{\mathrm{thino}}\exp\left(-\frac{t}{TC}\right), \tag{10-3}$$

where $t = i\Delta t$ is the time at the i-th impact and Δt = 2 x 10^3 years/$N_{\mathrm{total,BG}}$. Here, we used TC = 71 years, which corresponds to the value for a thin layer with a thickness of <0.3 mm (Table 7.1). The number of microbes protected by the ejecta-deposit layer N_{layer} at the i-th impact can be expressed as

$$N_{\mathrm{layer}} = \sigma_{\mathrm{thin}}(t)S_{\mathrm{shield}}. \tag{10-4}$$

The ratio $\Sigma N_{\mathrm{layer}}/\Sigma S_{\mathrm{shield}}$ yields the averaged-microbial-column density of the covered-microbial thin layer $\sigma_{\mathrm{thin,ave}}$ at the present on Phobos and Deimos as 1.0 x 10^{-6} CFU/cm^2 and 1.1 x 10^{-6} CFU/cm^2, respectively. By comparing with σ_{thino}, we found that the >95% of the microbes in the thin microbial layer is sterilized before they are covered by the ejecta blanket.

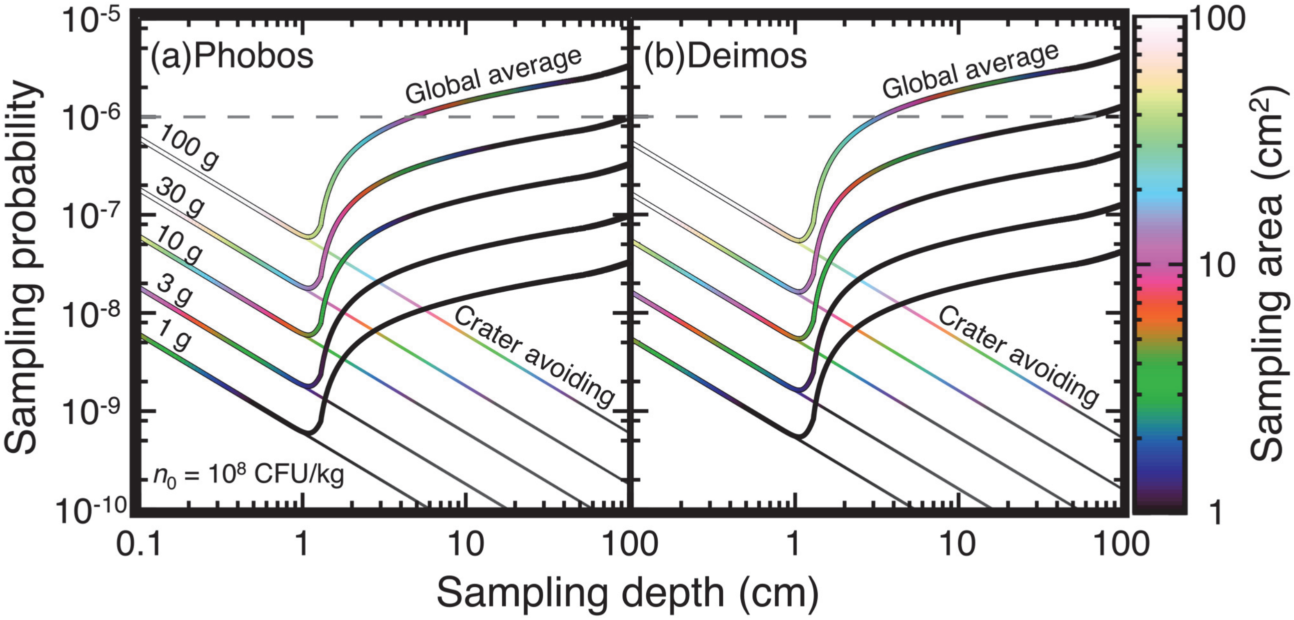

Fig. 10-2 The sampling probability of the microbes from the surface on each Phobos (a) and Deimos (b) as functions of sampling depth, area, and mass. The selected sampling masses are shown beside each of the lines. The Req-10 criterion is shown as the grey dashed horizontal line. The curves are the global-averaged probabilities including the Mars-rock craters. The straight lines on this log-log plot are the sampling probability avoiding the Mars-rock craters.

Finally, we discuss the sampling probability P_s of the microbes in the case of random sampling from somewhere on each of the moons. According to REQ-10, the boundary between the two categories, which are "Restricted" and "Un-restricted" Earth-return mission, $P_s = 10^{-6}$ as mentioned in Section 1. The sampling probabilities of the microbes from the Mars-rock craters and the covered-microbial thin layer $P_{s,crater}$ and $P_{s,layer}$ are given by

$$P_{s,crater} = P_{crater}\eta(t, H)n_{cratero}M_s, \tag{10-5}$$

and

$$P_{s,layer} = P_{layer}\sigma_{thin,ave}S_s, \tag{10-6}$$

where $\eta(t, H)$ is the survival rate for the radiation at a given depth and time listed in Table 7-2, $M_s = \rho_t S_S L_s$ is sampling mass, S_S is sampling area, and L_S is sampling depth. The sum of $P_{s,crater}$ and $P_{s,layer}$ is P_s. If we chose a sampling mass, the relation between S_S and L_S is determined uniquely. Figures 10-2 show P_s on Phobos and Deimos as functions of sampling area, depth and mass. The five different sampling masses were used in the calculation. If we choose M_s = 100 g, we could collect the regolith down to ~5 cm for Phobos and to ~3 cm for

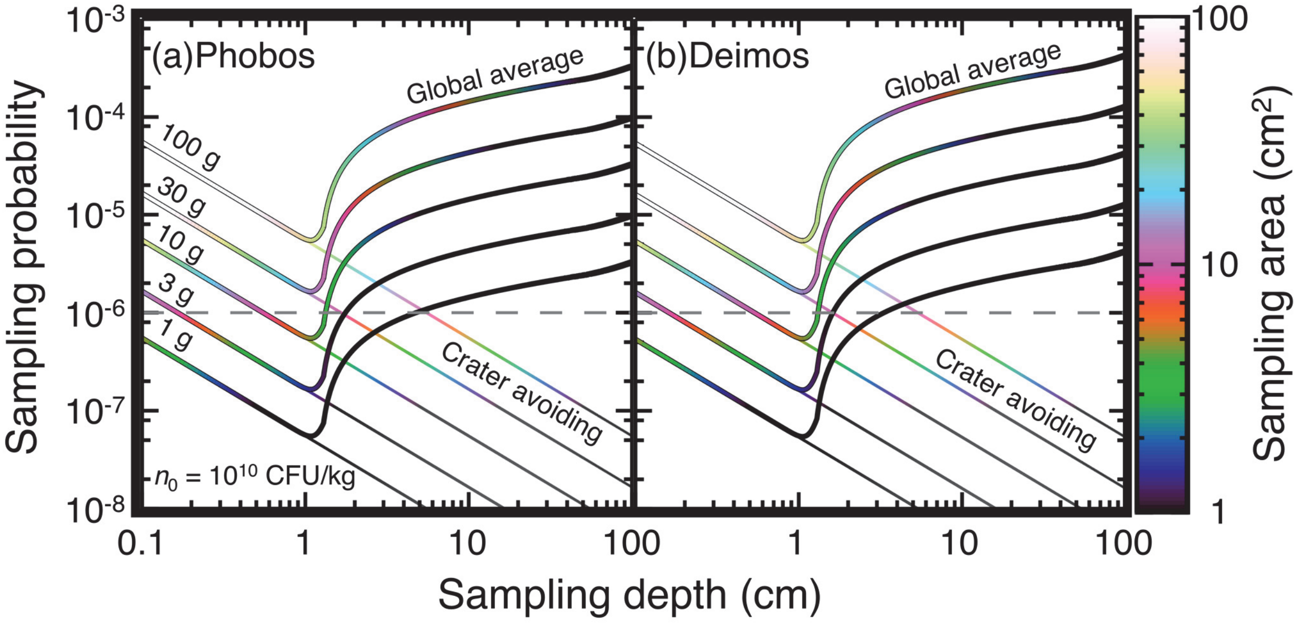

Fig. 10-3 Same as Figure 10-2 except that $n_{Mars} = 10^{10}$ CFU/kg was used and that the Y-axis is 2-orders shifted to the upward.

Deimos in the category of the Un-restricted Earth-return mission. These results lead to an interesting conclusion that the microbial contamination on Deimos is a little more severe than that on Phobos although Deimos is located much more far from Mars than Phobos.

If we could avoid the Mars-rock craters during the operation of sample collections, P_s becomes $P_s = P_{s,layer}$ displayed on Fig. 10-2 as straight lines. In this case, P_s monotonically decreases with increasing sampling depth because the microbes in the thin layer are diluted by the regolith particles. Thus, the limitation about the sampling depth could be removed. By substituting $P_s = P_{s,layer} = 10^{-6}$, the allowable sampling surface area on each of Phobos and Deimos can be obtained to be 9.1 x 10^2 cm^2 and 9.9 x 10^2 cm^2, which are obviously large enough to design boring-type sampling instruments.

In this study, we assumed that the initial microbe density on Mars is $n_{Mars} = 10^8$ CFU/kg based on the measurement of the Yungay area in the Atacama Desert, where is thought to be the best area in Mars analogs on the current Earth, as mentioned in Section 3. However, it is reported that the other areas in the Atacama Desert have a higher microbe density up to 10^{10} CFU/kg. Thus, we conducted a sensitivity analysis by changing the initial microbe density. Since the survival rates pertaining to both impact- and radiation-induced sterilization processes are scaled by the initial microbe density (Eqs. (6-2), (7-1), and (10-3)), we calculated P_s at $n_{Mars} = 10^{10}$ CFU/kg by using the 100-fold microbe densities, including $n_{crater}(t,H) = \eta(t, H)n_{cratero}$ and $\sigma_{thin,ave}$, and the same values of P_{crater}, P_{layer}, and $\eta(t, H)$. Figure 10-3 is the same as Figure 10-2 except that $n_{Mars} = 10^{10}$ CFU/kg was used and that the Y-axis is 2-orders shifted to the upward. Although this figure is equivalent to the Figure 10-2 if we adjusted the REQ-10 criterion to $P_s = 10^{-8}$ in Figure 10-2, this type of a graphical comparison would be useful. We found that the allowable sampling depth is limited only down to ~1 cm in the category of the Un-restricted Earth-return mission. Thus, we should distinguish the Mars-rock craters produced at >0.1 Myr ago and should avoid them during the operations of sample collections to extend the sampling depth down to > 1 cm in the category.

10.2. Contribution of Unrecognized Crater Events

Since the global catalog of Martian craters statistically complete to diameters larger than 1 km has been already presented [e.g., Robbins and Hynek, 2012], there is a little possibility that missing craters larger than 2 km in diameter, which is the minimum diameter contributing to the microbe transport [e.g., Artemieva and Ivanov, 2004], have been still existed. It, however, may be informative to examine the effects of potential recent crater-forming events on the sampling probability. Here, the diameter of such imaginary crater was set to 10 km, which is equivalent to the size of the Zunil crater. The crater chronology model on Mars has been statistically constructed based on the Lunar and Martian crater SFDs [e.g., Neukum et al., 2001]. The chronology model allows us to examine the expected number of craters with a given diameter at a given time [e.g., Hartmann, 2005]. The number is equivalent to the event probability P_{event} at a given surface age. Here, we examine the effects of a possible-missing Zunil-sized crater on the sampling probability from Phobos by considering the event probability. In a statistical sense, Zunil-sized craters are expected to be formed every ~1 Myr [e.g., Hartmann, 2005]. Thus, P_{event} is only 0.1 if the Zunil crater was actually produced at 0.1 Myr ago. Although we used 0.1 Myr as the formation age of the Zunil crater to do a risk assessment severely, the estimated age of the Zunil is ranged from 0.1 to 1 Myr [e.g., Hartmann, 2005]. Since the impact flux onto Mars in past 3 Gyr is nearly constant [e.g., Neukum et al., 2001], we could easily estimate P_{event} for Zunil-sized unfound craters at any values of the surface age. For example, P_{event} at 3 kyr is 3×10^{-3}.

We used the data in the "Ramdom" case from the orbital calculations described in Section 8 as the v_{imp} and θ_{imp} distributions for the Mars rocks from an imaginary unfound crater because the location of the crater is unknown. The transported mass of the Mars rocks from Zunil-sized craters was estimated to be 8.3×10^5 kg in the random case. By using the v_{imp} and θ_{imp} distributions, the averaged survival rate for the impact-induced sterilization ξ_{ave} and the averaged fraction of projectile retention ψ_{ave} are estimated to be 6.7×10^{-4} and 0.29, respectively. The sampling probability of the microbes transported from a unfound crater could be obtained as

$$P_s = P_{\text{event}} P_{s,\text{crater}} + P_{s,\text{layer}}. \tag{10-7}$$

In our model, $P_{s,\text{layer}}$ does not depend on the formation age of the Martian crater causing the microbe transportation because it is determined only by the background impacts during 2×10^3 years after the crater formation. Figure 10-4 is the same as Fig. 10-2 except that the calculated results for unfound Zunil-sized crater at six different formation ages ranged from 3 kyr to 1 Myr are shown and that two selected M_s = 60 g (a) and 100 g (b) are only displayed here. Since the survival rate for the radiation $\eta(t,H)$ and $P_{\text{event}}(t)$ are competitive in the calculation of the sampling probability, the sampling probability exhibits a complex behavior against the change in the formation age. Nevertheless, we could rule out the risk of the microbial contamination from such unfound crater down to ~10 cm from the surface of Phobos if the sampling mass could be limited to <60 g.

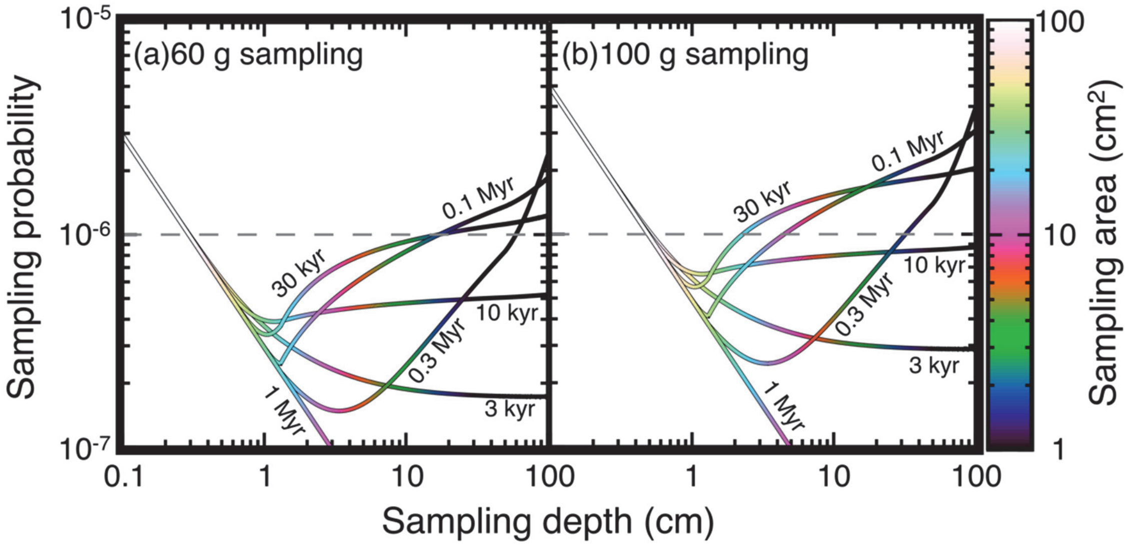

Fig. 10-4 Same as Fig. 10-2 except that the calculated results for unfound crater. (a) *Ms* = 60 g and (b) *Ms* = 100 g. The formation ages are shown beside the lines.

11. Comparison to Martian Meteorites on Earth

According to the analysis described above, a question arises:

> *Is Earth recently contaminated by Martian microorganisms transported with Mars meteorites?*

The answer may be ***Yes***, provided that the Martian moons are recently contaminated by Martian microorganisms by Mars ejecta through the physical processes considered in this study. The similar idea has already been argued by Mileikowsky et al. (2000) who conducted a detailed analysis on natural transfer of viable microbes from Mars to Earth. In this section, natural transfer of viable microbes is reanalyzed according to the same physical models used to assess microbial contamination of the Martian moons. Comparison is made between the risk for sample return from the Martian moons and natural transfer of Mars meteorites.

Potential microbial density on the Martian surface is assumed to be 10^8 CFU/kg (Sec. エラー！参照元が見つかりません。). Mars ejecta produced in a Mars crater event have potential microbial density of 10^7 CFU/kg, since microbial survival rate is 0.1 for hypervelocity impact sterilization during Mars ejecta formation (Sec. 4). Since Mars ejecta arriving at Earth should have initial velocities higher than the escape velocity, which is 5.03 km/s for Mars, aerodynamic heating during hypersonic flight in Martian atmosphere is expected to higher than that for Mars ejecta arriving at the Martian moons. However, as shown in Table エラー！参照元が見つかりません。, sterilization by aerodynamic heating quickly loses effect as the diameter of Mars ejecta increases. As with the case of Mars ejecta arriving at the Martian moons, those having a diameter greater than 0.1 m, which can leave the Martian atmosphere, are hardly sterilized. Above all, Mars ejecta transported to Earth have a diameter greater than 0.1 m and a microbial density of 10^7 CFU/kg in the initial state.

Table 11-1 List of latest Martian meteorites having cosmic-ray exposure ages less than 1 Myr (Aoudjehane et al., 2012; Nishiizumi et al., 2011; Park et al., 2003; Schwenzer et al., 2007; Wieler et al., 2016).

Martian meteorite	Cosmic-ray exposure ages (Myr)	Mass (kg)
EETA 79001	~ 0.6	7.94
NWA 4925	~ 0.7	0.282
Sayh al Uhaymir 005	~ 0.9	1.344
NWA 1195	~ 1.0	0.315
NWA 5789	~ 1.0	0.049
NWA 6162	~ 1.0	0.089
Tissint	~ 1.0	7-11
NWA 2046	~ 1.0	0.063
NWA 2626	~ 1.0	0.0311
Dar al Gani 476	~ 1.0	2.02

Mars ejecta are expected to be sterilized by radiation during an interplanetary cruise from Mars to Earth. According to the cosmic-ray exposure ages of the major Martian meteorites reviewed by Nyquist et al. (2001), and by Eugster et al. (2006) as well, Martian meteorites are considered to arrive at Earth within 0.5 to 20 Myr after departure from Mars. This result agrees well with the result of orbital calculations by Gladman (1996), which reported that approximately 20% of Mars ejecta arrive at Earth within 1 Myr from formation. The major Martian meteorites which are considered to be recently generated on the Martian surface are summarized in Table 11-1. Here, the cosmic-ray exposure age can be regarded as the age from generation. It is found that not quite a few number of Martian meteorites are younger than 1 Myr. The total mass of meteorites listed in Table 11-1 amounts to 19.2 kg. Because of their ages, a portion of the meteorites in Table 11-1 may originate from the Zunil crater event.

As a representative case study, let us consider a Martian meteorite having a 0.1-m diameter, which is generated 1 Myr ago on the Martian surface. If mass density is assumed as 2.0×10^3 kg/m^3, mass of the meteorite is $4\pi \times 0.05^3/3 \times 2\times10^3 = 1.0$ kg. Since Mars ejecta have a microbe density of 10^7 CFU/kg on their departure, the meteorite has 10^7 microbes in total. After an interplanetary cruise of 1 Myr before arrival at Earth, microbes are sterilized by radiation. The radiation sterilization model (Sec. 7) applied to a spherically symmetric form under consideration yields a distribution of microbe number shown in Fig. 11-1. Thus, the probability that the meteorite contains microorganisms is 4.1×10^{-3} on arrival at Earth. It should be noted that the meteorite is more likely to be unsterilized at the center.

The meteorite enters into the Earth atmosphere where it undergoes aerodynamic heating. According to kinetics of orbital transfer from Mars to Earth, the atmospheric entry velocity of the meteorite is as high as 12 km/s, similar to HAYABUSA and Stardust sample return capsules. With assumptions of an atmospheric entry velocity of 12-km/s and a flight path angle of -10 degrees, microbial survival rate for aerodynamic heating is estimated to be 0.013 by using the approaches of Sec. エラー! 参照元が見つかりません。 applied to Earth

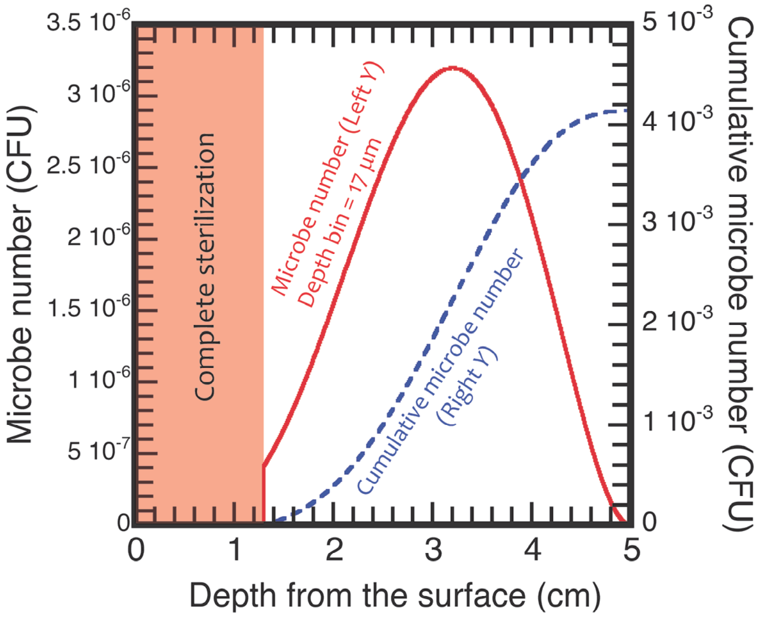

Fig. 11-1 Distribution of microbes in a 0.1-m Martian meteorite after radiation sterilization for 1 Myr.

entry. Thus, the meteorite has a contamination probability of 4.1×10^{-3} x 0.013 = 5.3×10^{-5} before touch down. It should be noted that the center to aftbody region of the meteorite is more likely to maintain microbes without sterilization due to low temperature, as suggested in Fig. 5-7. Unlike the case of Mars ejecta transported to the Martian moons, the meteorite is completely decelerated to the terminal velocity by the aerodynamic drag, so that no impact sterilization is expected when it touches down the ground. In this way, probability that the meteorite contains one microbe is 5.3×10^{-5} on the ground, which is more than 50 times higher than that required for sample return from the Martian moons.

The above case study gives a very conservative estimation of microbial contamination probability of Martian meteorites transported to Earth. For example, a Tissint-like meteorite, which is 10 kg and 0.257 m in diameter, is expected to have a microbial contamination probability at the order of 10^{-1}. It is clear that the Martian meteorites listed in Table 11-1 are only the tip of the iceberg, and a much larger number of Martian meteorites are considered to have been transported to Earth with considerable number of microbes.

According to COSPAR planetary protection policy (PPP), determination as to whether a sample return mission is classified "Restricted Earth return" or not shall address the six questions, the sixth of which goes

> *Does the preponderance of scientific evidence indicate that there has been a natural influx to Earth, e.g., via meteorites, of material equivalent to a sample returned from the target body?*

Based on the estimation of microbial contamination probability of Martian meteorites obtained in this study, and on the preceding study of Mileikowsky et al. (2000), it is clear that the answer to the sixth question is ***Yes***. For this reason, associated with the fact that samples collected on the Martian moons can have microbial contamination probabilities less than 10^{-6}, it is considered that sample return from the Martian moons is classified as ***Unrestricted Earth return***.

12. Conclusions

- Transportation of Mars ejecta with potential microbial contamination to Martian moons is simulated according to major five crater events and potential unrecognized crater events that may have occurred in past 10 Myr.
- Mars ejecta impacting on Phobos and Deimos form craters and break into fragments. The fragments are partly sterilized by impact sterilization. Some portion of the fragments remain in the crater, forming risky areas with relatively high microbial density. The rest of fragments, which are small in diameter, are finally scattered over the surface of Martian moons, forming a contaminated layer of submillimeter thickness.
- The contaminated areas are sterilized by radiation over time. The microbial density in the crater decreases slowly because of large thickness, while that of the contaminated layer quickly decreases within 2 Kyr in general. However, a small portion of the contaminated moon's surface is covered before radiation sterilization with thick layers of regolith produced by continuous meteoroid impacts on the Martian moons. Such thick layers slow down radiation sterilization, leaving risky areas outside the craters.
- Hypervelocity impact and radiation play major roles in sterilization of potential microbes transported from the Martian surface. It is strongly recommended to validate accuracy of the hypervelocity impact sterilization model developed in this study in the velocity range beyond 2 km/s.
- Microbial contamination probability of samples collected on Deimos is almost the same as that on Phobos.
- Microbial contamination probability of collected samples can be easily made below 10^{-6} by choosing appropriate sampling approaches. One example is to collect 100-g samples with a restriction of boring depth shorter than 5 cm. Another example is to limit mass of samples below 30 g. In this case, no restriction on sampling depth applies.
- Microbial contamination probability due to natural transfer by Martian meteorite is several orders of magnitude higher than that of sample return from the Martian moons, suggesting an apparent evidence of a natural influx from Mars including viable microbes.
- From the above results, sample return from the Martian moons can be classified as Unrestricted Earth return.

Acknowledgements

A part of this research was conducted by using the iSALE computer program. We wish to acknowledge the developers of iSALE, including G. Collins, K. Wünnemann, B. Ivanov, J. Melosh, and D. Elbeshausen.

References

Aislabiea, J. M., Chhourb, K-L., Saulb, D. J., Miyauchib, S., Aytonb, J., Paetzoldc, R. F., Balksd, M. R., 2006. Dominant bacteria in soils of Marble Point and Wright Valley, Victoria Land, Antarctica. Soil Biology and Biochemistry, 38, 3041-3056.

Allen, R. T., 1967. Equations of state of rocks and minerals. interim report to DASA under contract DA 49-146-XZ-462. *General Dynamics Report #*GA MD-7834.

Amsden, A. A., Ruppel, H. M., and Hirt, C. W., "SALE: a Simplified ALE Computer Program for Fluid Flow at All Speeds," Los Alamos National Laboratories Report, LA-8095, (1980).

Andert, T. P., Rosenblatt, P., Pa¨tzold, M., Ha¨usler, B., Dehant, V., Tyler, G. L., and Marty, J. C., 2010. Precise mass determination and the nature of Phobos. Geophys Res Lett 37, doi:10.1029/ 2009GL041829.

Aoudjehane H. C., Avic G., Barrat J.-A., Boudouma O., Chen G., Duke M. J. J., Franchi I. A., Gattacceca J., Grady M. M., Greenwood R. C., Herd C. D. K., Hewins R., Jambon A., Marty B., Rochette P., Smith C. L., Sautter V., Verchovsky A., Weber P., and Zanda B., 2012. Tissint Martian meteorite: A fresh look at the interior, surface, and atmosphere of Mars. Science, 338, 765-788.

Artemieva, N., Ivanov, B., 2004. Launch of martian meteorites in oblique impacts. Icarus 171, 84-101.

Chappaz, L., Melosh, H. J., Vaquero, M., and Howell, K. C., 2013. Transfer of Impact Ejecta Material from the Surface of Mars to Phobos and Deimos. Astrobiology, 13, 963-980.

Connon, S. A., Lester, E. D., Shafaat, H. S., Obenhuber, D. C., and Ponce, A., 2007. Bacterial diversity in hyperarid Atacama Desert soils. Journal of Geophysical Research, 112, G04S17.

Daly, R. T. and Schultz, P. H., 2016. Delivering a projectile component to the vestan regolith. Icarus 264:9-19.

Drees, K. P., Neilson, J. W., Betancourt, J. L., Quade, J., Henderson, D. A., Pryor, B. M., and Maier, R. M., 2006. Bacterial Community Structure in the Hyperarid Core of the Atacama Desert, Chile. Applied and Environmental Microbiology, 72, 7902-7908.

Duvall, A., Justus, C., and Keller, V., 2005. Global Reference Atmospheric Model (GRAM) Series for Aeroassist Applications. AIAA Paper 2005-1239, 43rd AIAA Aerospace Sciences Meeting and Exhibit, Reno, Nevada, USA.

Ebert, M., Hecht, L., Deutsch, A., Kenkmann, T., Wirth, R., and Berndt, J., 2014. Geochemical processes between steel projectiles and silica-rich targets in hypervelocity impact experiments. Geochimica et Cosmochimica Acta 133, 257-279.

Elbeshausen, D., Wunnemann, K., and Collins, G. S., 2013. The transition from circular to elliptical impact craters. Journal of Geophysical Research 118, 1-15, doi:10.1002/2013JE004477.

Eugster, O., Herzog, G. F., Marti, K., and Caffee, M. W., 2006. Irradiation Records, Cosmic-Ray Exposure Ages, and Transfer Times of Meteorites," in Meteorites and the Early Solar System II, edited by Lauretta, D. S. and McSween Jr., H. Y., University of Arizona Press, Tucson, 829.

Fritz, J., Greshake, A., and Fernandes, V. A., 2017. Revising the shock classification of meteorites. Meteoritics & Planetary Science, 52, 1216-1232.

Fujita, K., Sumi, T., Yamada, T., and Ishii, N., 2006. Heating Environments of a Venus Entry Capsule in a Trail Balloon Mission. Journal of Thermophysics and Heat Transfer, 20, 507–516.

Fujita, K., Matsuyama, S., and, Suzuki, T., 2012. Prediction of Forebody and Aftbody Heat Transfer Rate for Mars Aerocapture Demonstrator. AIAA Paper 2012-3001, 43rd Thermophysics Conference, New Orleans, Louisiana, USA.

Genda, H., Kurosawa, K., Okamoto, T., Hydrocode modeling of the spallation process during hypervelocity oblique impacts. in prep.

Gilichinsky, D. A., Wilson, G. S., Friedmann, E. I., McKay C. P., Sletten, R. S., Rivkina, E. M., Vishnivetskaya, T. A., Erokhina, L. G., Ivanushkina, N, E., Kochkina, G. A., Shcherbakova, V. A., Soina, V. S., Spirina, E. V., Vorobyova, E. A., Fyodorov-Davydov, D. G., Hallet, B., Ozerskaya, S. M., Sorokovikov, V. A., Laurinavichyus, K. S., Shatilovich, A. V., Chanton, P., Ostroumov, V. E., and Tiedje, J. M., 2007. Microbial populations in Antarctic permafrost: biodiversity, state, age and implication for astrobiology. Astrobiology, 7, 275–311.

Gladman, B. J., Burns, J. A., Duncan, M., Lee, P., and Levison, H. F., 1996. The exchange of impact ejecta between terrestrial planets. Science 271, 1387.

Glavin, D. P., Cleaves, J., Schubert, M., Aubrey, A., Bada, J. L., 2004. New Method for Estimating Bacterial Cell Abundances in Natural Samples by Use of Sublimation. Applied and Environmental Microbiology, 70, 5923-5928.

Golombek, M., Bloom, C., Wigton, N., and Warner, N., 2014. Constraints on the age of Corinto crater from mapping secondaries in Elysium planitia on Mars. LPS XXXXV, 1470.

Goordial, J., Davila, A., Lacelle, D., Pollard, W., Marinova, M. M., Greer, C. W., DiRuggiero, J., McKay, C. P., and Whyte, L. G., 2016. Nearing the cold-arid limits of microbial life in permafrost of an upper dry valley, Antarctica. The ISME Journal, 10, 1613-1624.

Hartmann, W. K., 2005. Martian cratering. 8. Isochron refinement and the chronology of Mars. Icarus, 174, 294–320.

Hartmann, W. K., Quantin, C., Werner, S. C., and Popova, O., 2010. Do young martian ray craters have ages consistent with the crater count system? Icarus, 208, 621-635.

Hawke, B.R., Blewett, D.T., Lucey, P.G., Smith, G.A., Bell, J.F., Campbell, B.A., and Robinson, M.S., 2004. The origin of lunar crater ray. Icarus 170, 1-16.

Hirata, N., 2017. Spatial distribution of impact craters on Deimos. Icarus 288, 69-77.

Housen, K. R., Schmidt, R. M., and Holsapple, K. A., 1983 Crater ejecta scaling laws: Fundermental forms based on dimensional analysis. Journal of Geophysical Research 88, 2485-2499.

Holsapple, K. A. and Schmidt, R. M., 1982. On the scaling of crater dimensions: 2. Impact processes. Journal of Geophysical Research, 87, 1849-1870.

Hyodo R. and Charnoz S., 2017. Dynamical Evolution of the Debris Disk after a Satellite Catastrophic Disruption around Saturn. The Astronomical Journal, 154:34.

Hyodo, R., Genda, H., Charnoz, S., Pignatale, F. C. F., Rosenblatt, P., 2018. On the impact origin of Phobos and Deimos. IV. Volatile depletion. The Astrophysical Journal 860, 150(10pp).

Hyodo, R., Kurosawa, K., Genda, H., and Fujita, K., On the delivery of impact ejecta from Mars to Phobos and Deimos: Revisited. in prep.

Hyodo, R., Ohtsuki, K., and Takeda, T., 2015. Formation of multiple-satellite systems from low-mass circumplanetary particle disks. The Astrophysical Journal, 799:40.

Ito, T. and Malhotra, R., 2006. Dynamical transport of asteroid fragments from the ν6 resonance. Advances in Space Research, 38, 817-825.

Ivanov, B. A., Deniem, D., and Neukum, G., 1997. Implementation of Dynamic Strength Models into 2-D Hydrocodes: Applications for Atmospheric Breakup and Impact Cratering. International Journal of Impact Engineering 20, 411.

Ivanov, B. A., Melosh, H. J., and Pierazzo, E., 2010. Basin-Forming Impacts: Reconnaissance Modeling. In Large Meteorite Impacts and Planetary Evolution IV, edited by Gibson R. L. and Reimold W. U., Special Paper 465, The Geological Society of America, 29.

Johnson, B. C. and Melosh, H. J., 2013. Formation of melt droplets, melt fragments, and accretionary impact lapilli during a hypervelocity impact. Icarus, 228, 347-363.

Justus, C. G., Duvall, A., and Keller, V. W., 2005. Atmospheric Models for Mars Aerocapture. AIAA Paper 2005-4106, 41st AIAA/ASME/SAE/ASEE Joint Propulsion Conference and Exhibit, Tucson, Arizona, USA.

Kurosawa, K. and Genda, H., 2018. Effects of Friction and Plastic Deformation in Shock-Comminuted Damaged Rocks on Impact Heating. Geophysical Research Letters, 45, 620-626.

Kurosawa, K., Okamoto, T., and Genda, H., 2018. Hydrocode modeling of the spallation process during hypervelocity impacts: Implications for the ejection of Martian meteorites. Icarus, 301, 219-234.

Kurosawa, K., Genda, H., Hyodo, R., Yamagishi, A., and Fujita, K., The fate of microbe transported from Mars to Phobos. in prep.

Lester, E. D., Satomi, M., and Ponce, A., 2007. Microflora of extreme arid Atacama Desert soils. Soil Biology and Biochemistry, 39, 704-708.

Lucy, L. B., 1977. A numerical approach to the testing of the fission hypothesis. The Astronomical Journal, 82, 1013-1024.

Maier, R. M., Dress, K. P., Neilson, J. W., Henderson, D. A., Quade, J., and Betancourt, J. L., 2004. Microbial Life in the Atacama Desert. Science, 306, 1289-1290.

Malin, M. C., Edgett, K. S., Posiolova, L. V., McColley, S. M., and Noe Dobrea, E. Z., 2006. Present-day impact cratering rate and contemporary gully activity on Mars. Science, 314, 1573-1573.

McEwen, A. S., Preblich, B.S., Turtle, E. P., Artemieva, N. A., Golombek, M. P., Hurst, M., Kirk, R. L., Burr, D. M., Christensen, P. R., 2005. The rayed crater Zunil and interpretations of small impact craters on Mars. Icarus, 176, 351–381.

McKinnon, W. B., Chapman, C. R., and Housen, K. R., 1991. Cratering of the Uranian satellites, in Uranus, edited by Bergstralh, J. T., Miner, E. D., and Matthews, M. S., University of Arizona Press, Tucson, 629-692.

Melosh, H. J., 1989. Impact cratering: A geologic process. Oxford University Press, New York.

Melosh, H. J., 2011. Material Transfer from the Surface of Mars to Phobos and Deimos. Final Report: NNX10AU88G, Purdue University.

Melosh, H. J. and Ivanov, B. A., 2018. Slow impacts on strong targets bring on the heat. Geophysical Research Letters, 45, 2597-2599.

Melosh, H. J. and Vickery, A. M., 1989. Impact erosion of the primordial atmosphere of Mars. Nature 338, 487-489.

Mizutani, H., Takagi, Y., and Kawakami, S., 1990. New scaling laws on impact fragmentation. Icarus 87, 307-326.

Mileikowsky, C., Cucinotta, F. A., Wilson, J. W., Gladman, B., Horneck, G., Lindegren, L., Melosh, J., Rickman, H., Valtonen, M., and Zheng, J. Q., 2000. Natural Transfer of Viable Microbes in Space: 1. From Mars to Earth and Earth to Mars. Icarus, 145, 391–427.

Monaghan, J.J., 1992. Smoothed particle hydrodynamics. Annual Review of Astronomy and Astrophysics, 30, 543–574.

Murray, C. D. and Dermott, S. F., 1999. Solar System Dynamics, Cambridge University Press, Cambridge, UK.

Navarro-González, R., Rainey, F. A., Molina, P., Bagaley, D. R., Hollen, B. J., de la Rosa, J., Small, A. M., Quinn, R. C., Grunthaner, F. J., Cáceres, L., Gomez-Silva, B., and McKay, C. P., 2003. Mars-Like Soils in the Atacama Desert, Chile, and the Dry Limit of Microbial Life. Science, 302, 1018-1021.

Neukum, G., Ivanov, B. A., Hartmann, W. K., 2001. Cratering records in the inner solar system in relation to the lunar reference system. Space Science Review 96, 55–86.

Nishiizumi K., Nagao K., Caffee M. W., Jull A. J. T., and Irving A. J., 2011. Cosmic-ray exposure chronologies of depleted olivine-phyric shergottites. Lunar Planet. Sci. 42, Lunar Planetary Institute, Houston, #2371 (abstract).

Nyquist, L. E., Bogard, D. D., Shih, C.-Y., Greshake, A., Stöffler, D., and Eugster, O., 2001. Ages and Geologic Histories of Martian Meteorites. Space Science Reviews 96, 105.

Park, J., Bogard, D. D., Mikouchi, T., and McKay, G. A., 2008. Dhofar 378 Martian Shergottite: Evidence of Early Shock Melting. Journal of Geophysical Research 113, E08007.

Park, J., Okazaki, R., and Nagao, K., 2003. Noble gas studies of Martian meteorites: Dar al Gani 476/489, Sayh al Uhaymir 005/060, Dhofar 019, Los Angeles 001 and Zagami. Lunar Planet. Sci. 34, Lunar Planetary Institute, Houston, #1213 (abstract).

Parkos, D., Pikus, A., Alexeenko, A., and Melosh, H. J. 2018. HCN Production via Impact Ejecta Reentry During the Late Heavy Bombardment. Journal of Geophysical Research: Planets, 123, 892-909.

Patel, M., Gow, J., Paton, S., and Truscott, P., 2017. Test report on the irradiation inactivation tests results. SterLim-OU-TN15.

Patel, M., Pearson, V., Summers, D., Evans, D., Bennet, A., and Truscott, P., 2018. Sterilization Limits for Sample Return Planetary Protection Measures (SterLim). Presentation to the Committee on the Review of Planetary Protection Requirements for Sample Return from Phobos and Deimos, ESA contract no. 4000112742/14/NL/HB.

Pike, R. J., 1988. Geomorphology of impact craters on Mercury. in Mercury, edited by Balogh, A., Ksanfomality, L. and von Steiger, R., University of Arizona Press, Tucson, 165-273.

Preblich, B. S., McEwen, A. S., and Studer, D. M., 2007. Mapping rays and secondary craters from the Martian crater Zunil. Journal of Geophysical Research E: Planets, 112, E05006.

Ramsley, K. R. and Head, J. W., 2013. Mars impact ejecta in the regolith of Phobos: Bulk concentration and distribution. Planetary and Space Science, 87, 115-129.

Robbins, S. J. and Hynek, B. M., 2012. A new global database of Mars impact craters ≥1 km: 1. Database creation, properties, and parameters. Journal of Geophysical Research, 117, E05004, doi:10.1029/2011JE003966.

Schmedemann, N., Michael, G. G., Ivanov, B. A., Murray, J. B., and Neukum, G., 2014. The age of Phobos and its largest crater, Stickney. Planetary and Space Science 102, 152-163.

Schmidt, R. M. and Housen, K.R., 1987. Some recent advances in the scaling of impact and explosion cratering. International Journal of Impact Engineering, 5, 543-560.

Shoemaker, E. M., 1962. Interpretation of lunar craters. in Physics and Astronomy of the Moon, edited by Z. Kopal, pp. 283–359, Academic, San Diego, CA, USA.

Schwenzer, S. P., Herrmann, S., Mohapatra, R. K., and Ott, U., 2007. Noble gases in mineral separates from three shergottites: Shergotty, Zagami, and EETA79001. Meteoritics and Planet. Sci., 42, 387-412.

Summers, D., 2017. Evaluation of the level of assurance that no unsterilized martian material naturally transferred to Phobos (and Deimos) is accessible to a Phobos (and Deimos) sample return mission. SterLim-Ph2-TAS-TN21.

Takenouchi, A., Mikouchi, T., and Kogure, T., 2017. Mineralogical study of brown olivine in Northwest Africa 1950 shergottite and implications for the formation mechanism of iron nanoparticles. Meteoritics & Planetary Sciences, 52, 2491-2504.

Tanaka, H., Inaba, S., and Nakazawa, K., 1996. Steady-state size distribution for the self-similar collision cascade. Icarus 123, 450-455.

Tauber, M. E., Bowles, J. V., and Yang, L., 1990. Use of Atmospheric Braking During Mars Missions. Journal of Spacecraft and Rockets, 27, 514–521.

Tauber, M. E. and Sutton, K., 1991. Stagnation-Point Radiative Heating Relations for Earth and Mars Entries. Journal of Spacecraft and Rockets, 28, 40–42.

Tillotson, J.H., 1962. Metallic Equations of State for Hypervelocity Impact. General Atomic, Division of General Dynamics, John Jay Hopkins Laboratory for Pure and Applied Science.

Thomas, P. C., 1998. Ejecta emplacement on the Martian Satellites. Icarus 131, 78-106.

Tornabene, L. L., Moersch, J. E., McSween, H. Y., McEwen, A. S., Piatek, J. L., Milam, K. A., and Christensen, P. R., 2006. Identification of large (2–10 km) rayed craters on Mars in THEMIS thermal infrared images: Implications for possible Martian meteorite source regions. Journal of Geophysical Research E: Planets, 111, E10006.

Werner, S.C., Ody, A., and Poulet, F., 2014. The source crater of Martian Shergottite meteorites. Science 343, 1343–1346.

Wieler, R., Huber, L., Busemann, H., Seiler, S., Leya, I., Maden, C., Masarik, J., Meier, M. M. M., Nagao, K., Trappitsch, R., and Irving, A. J., 2016. Noble gases in 18 Martian meteorites and angrite Northwest Africa 7812- Exposure ages, trapped gases, and a re-evaluation of the evidence for solar cosmic ray-produced neon in shergottites and other achondrites. Meteoritics and Planet. Sci., 51, 407-428.

Wünnemann, K., Collins, G. S., and Melosh, H. J., 2006. A Strain-Based Porosity Model for Use in Hydrocode Simulations of Impacts and Implications for Transient Crater Growth in Porous Targets. Icarus 180, 514.

Zahnle, K., Schenk, P., Levison, H. and Dones, L., 2003. Cratering rates in the outer solar system. Icarus, 163, 263–289.